Contrib Mineral Petrol (2016) 171:7
DOI 10.1007/s00410-015-1212-x

ORIGINAL PAPER

Clinopyroxene in postshield Haleakala ankaramite: 1. Efficacy of thermobarometry

Julia Hammer[1] · Samantha Jacob[1] · Benoit Welsch[1] · Eric Hellebrand[1] · John Sinton[1]

Received: 14 July 2015 / Accepted: 20 November 2015

Abstract Magma storage depth is a fundamental aspect of a volcano's magmatic plumbing system that may be resolved using mineral-melt thermobarometry, assuming crystal growth occurs at near-equilibrium conditions. We acquire major and minor element compositional analyses of whole rock, groundmass separates, and clinopyroxene in ankaramite erupted ca. 214 ka at Haleakala volcano to evaluate the efficacy of thermobarometry. Using various thermometer and barometer combinations, we obtain values of crystallization pressure (60–1500 MPa) that are generally consistent with those of previous studies, but find that the models most successful at recovering the conditions of relevant equilibrium experiments yield values at the low end of this range (≤950 MPa). We use quantitative EPMA spot analyses to transform X-ray element intensity maps into metal oxide concentrations maps and to produce qualitative pressure maps of whole crystals. The spatial context provided by this procedure reveals two compositionally distinct domain types not evident in the spot analysis data set, with median Na_2O contents differing by up to 26 % between domains. Na-rich domains represent putative crystallization pressures that are up to 365 MPa higher than Na-poor domains, within individual crystals. The presence of Na-rich domains associated with euhedral facets in contact with matrix is not consistent with concentric growth at near-equilibrium conditions of decreasing pressure, but rather co-crystallization of both domains under conditions of partial disequilibrium. Conservatively assuming that low-Na regions are less prone to kinetic partitioning, crystallization pressures for the Haleakala ankaramite correspond to crustal levels. We conclude that the reservoir supplying postshield eruptions at Haleakala has not deepened into the mantle, as was reported in a previous application of clinopyroxene thermobarometry to Haleakala's postshield magma (Chatterjee et al. 2005).

Keywords Ocean island volcanism · Clinopyroxene · Thermobarometry · Sector zoning

Introduction

The depth at which magma is stored beneath an eruptive center influences its composition, mineralogy, the dynamics of eruption, and ultimately the volcano's eruptive hazard potential. Determining the depths of magma storage regions is thus one component of establishing the geometry and time evolution of magmatic processes occurring in a volcanic plumbing system, and it is the pursuit of depth and process constraints at Haleakala with which this study is concerned.

Geophysical, geochemical, and geologic observations reveal that Hawaiian volcanoes in the shield building stage of their development are fed quasi-continuously by one or several magma reservoirs lying within the volcanic edifice, less than 6 km from the surface (Pietruszka et al. 2015; Poland et al. 2014; Ryan 1987; Tilling et al. 2014). The postshield stage, by comparison, is a transient state occurring between the period of high magmatic flux

Communicated by Gordon Moore.

Electronic supplementary material The online version of this article (doi:10.1007/s00410-015-1212-x) contains supplementary material, which is available to authorized users.

✉ Benoit Welsch
bwelsch@hawaii.edu

[1] Department of Geology and Geophysics, University of Hawaii, Honolulu, HI, USA

Published online: 15 December 2015

characterizing the shield building stage, and the subsequent quiescence as the volcano moves away from the underlying mantle hot spot (Macdonald et al. 1983). The postshield stage is therefore characterized by transitional behavior with respect to eruption frequency, effusive flux, and magma composition (Clague and Sherrod 2014; Macdonald and Powers 1968; Sinton 2005; Wolfe et al. 1997). Correlative information about the plumbing systems of postshield volcanoes, such as Haleakala and Hualalai, which have not erupted in the era of modern geophysics yet are undeniably active (Sherrod et al. 2003) must be sought using petrologic methods.

Determinations of magma reservoir conditions at postshield Hawaiian volcanoes are predicated on one or more related assumptions: (1) that the mineralogy of lavas preserves information about the pressure and temperature at which crystallization occurs; (2) that suites of whole rock lava compositions trace the path of a liquid line of descent, which is strongly influenced by the pressure at which magma crystallizes, and/or (3) that the compositions of individual mineral grains preserve a record of intensive conditions during the growth of the crystal. An example of the first approach, consistent with the observed increase in clinopyroxene stability with respect to olivine with increasing pressure (Mahood and Baker 1986; Yoder and Tilley 1962), is the inferred deep (17–19 km; >5–7 kbar) origin of clinopyroxene-rich lavas of Mauna Kea's postshield Laupahoehoe stage (Langenheim and Clague 1987; Wolfe et al. 1997). The second approach was applied by Bergmanis et al. (2000) to a set of late postshield Haleakala lavas using the MELTS algorithm (Ghiorso and Sack 1995). In that study, a liquid line of descent defined by whole-rock compositions constrain the pressure of magma differentiation to within-edifice values (3 kbar = 300 MPa ~10–11 km for an average crust density of 2900 kg m^{-3}). A third approach uses clinopyroxene-liquid thermobarometry (Chatterjee et al. 2005) applied to scoria from a crystal-rich pyroclastic deposit at the summit of Haleakala, notably recovering much greater pressures (4.4–11.2 kbar; up to 45 km) than Bergmanis et al. (2000) for products of the same volcanic stage.

We studied samples of an ankaramite lava flow from Haleakala Volcano (Hawaii), which has the advantage of being stratigraphically contextualized within the sequence of Hawaiian volcano development (Sherrod et al. 2003) and affiliated with rocks that are reasonably well studied (Bergmanis et al. 2000; Chatterjee et al. 2005; Chen et al. 1990). The flow contains a high fraction of large crystals of clinopyroxene that are partly weathered out into loose grains, providing a unique opportunity to observe surface morphologies and textures in three dimensions (detailed in Welsch et al. 2015). We report major element compositions of whole rocks and mechanically separated groundmass fractions for two hand samples, couple these data with spot analysis of clinopyroxene and olivine in petrographic thin sections, in order to extend the data base of postshield products at Haleakala, apply and evaluate thermobarometric calculations of crystallization pressure, and consider conflicting models of ankaramite generation at Haleakala Volcano.

Geologic setting

Maui is one of the youngest shield edifices formed by the hotspot track of Hawaii. The island belongs to the former "Maui Nui" group of subaerially continuous volcanoes including Lanai, Kahoolawe and Molokai, and is composed of two overlapping volcanoes: Mauna Kahalawai, the older West Maui volcano, and Haleakala, the younger East Maui volcano. Three lava units compose Haleakala volcano: (1) tholeitiic and alkali basalts from the late shield building stage (Honomanu > 0.96 Ma), (2) alkalic basalts, hawaiites, mugearites and ankaramites from an early postshield stage (Kula, 0.96–0.12 Ma) and (3) ankaramites, alkalic basalts and hawaiites from a stratigraphically distinct later postshield stage (Hana $\leq$ 0.12 Ma; Clague and Sherrod 2014; Macdonald et al. 1983; Macdonald and Katsura 1964; Naughton et al. 1980; Sherrod et al. 2006; Stearns and Macdonald 1942). Recent K–Ar age dating indicates that the Haleakala produced ca. 15 eruptive sequences in the past 1500 years (Sherrod et al. 2003). Post-caldera erosion and postshield volcanism are contemporaneous, indicating that no major eruptive hiatus has occurred and thus that Haleakala volcano is approaching its millionth year of postshield activity (Sherrod et al. 2003).

Ankaramites are important constituents of recent volcanism at Haleakala, with clinopyroxene-rich lavas and pyroclastics younger than 13,000 years erupted from the east rift zone, southwest rift zone, and Haleakala crater section (Sherrod et al. 2006). The volcano's most recent eruption produced the ankaramite Kalua o Lapa flow at A.D. 1420–1620 (Sherrod et al. 2006). These pyroclastic vent deposits and lavas have whole-rock compositions that would be classified as picrobasalts according to silica—alkali systematics, or as basanites following Coombs and Wilkinson (1969). However, they receive the designation "ankaramite" because they contain up to 60 vol% crystals, with clinopyroxene in excess of olivine (Lacroix 1916, 1923; Marsh 1981). This type of lava is notably prominent among ocean island volcanoes [e.g., Comores islands (Lacroix 1923), Crozet islands (Gunn et al. 1970), Vanuatu (Barsdell 1988; Barsdell and Berry 1990; Eggins 1993), and Azores (Genske et al. 2012)] as well as volcanic arcs [e.g., Sunda arc (Della-Pasqua and Varne 1997), Central Mexico (Ortiz Hernández 2000), Mariana (Kohut et al. 2006), and Srednogorie, Bulgaria (Georgiev et al. 2009)].

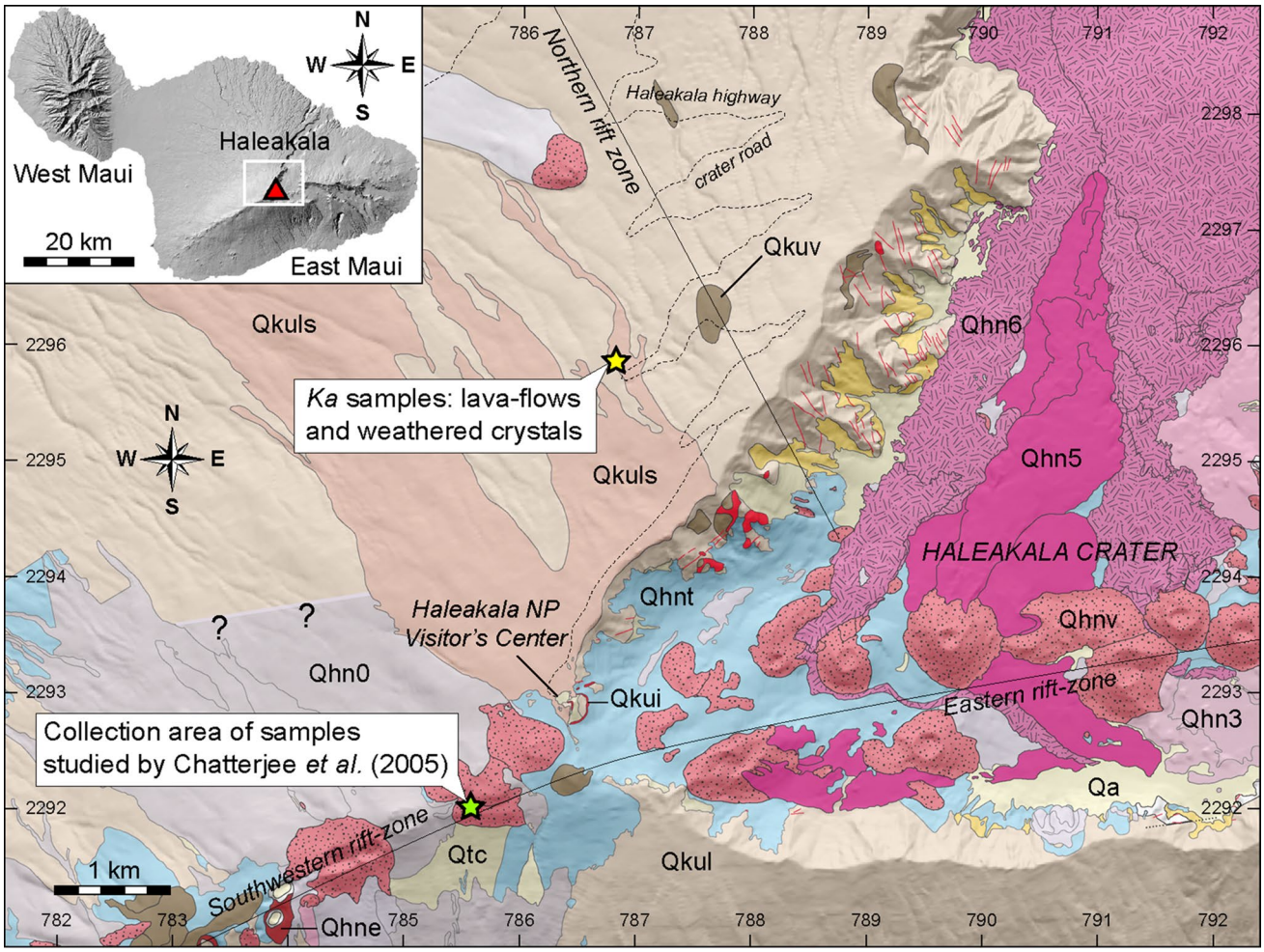

Fig. 1 Sampling site in at Haleakala volcano (GPS position 786,797; 2295,850 m UTM 4; units in the map are given in km UTM 4). Also represented the collection area of samples (Kolekole crater) studied by Chatterjee et al. (2005). Digital elevated model at http://www.soest.hawaii.edu/coasts/data/maui/dem.html. Geologic map after Sherrod et al. (2007). Qkui (intrusive rocks), Qkul (lava flows), Qkuls (summit ankaramites) and Qkuv (vent deposits) are Kula volcanics from Pleistocene. Qhne (explosion crater deposits), Qhnt (tephra deposit), Qhnv (vent deposits), Qhn0 (lavas flows at 50–140 ka), Qhn5 (lavas flows at 1.5–3 ka) and Qhn6 (lavas flows at <1.5 ka) are Hana volcanics from Holocene and Pleistocene. Qtc (talus and colluvium) and Qa (alluvium) from Holocene

Methods

Samples

Two fragments of lava, labeled Ka01 and Ka02, and numerous loose crystals of clinopyroxene were sampled from an ankaramite a'a flow near the summit of Haleakala Volcano, mapped as "ka" (Macdonald 1978) and later as Qkuls (Sherrod et al. 2007; Fig. 1). Dated at 214 ± 20 ka (Sherrod et al. 2003), this flow is among the youngest Kula volcanics on the western flank of the volcano and presumably emanated from a now-eroded vent near the Haleakala National Park Visitor's Center (Sherrod et al. 2007). The Qkuls samples share petrologic features with even younger ankaramites (128 ka) from the summit area of Haleakala (Chatterjee et al. 2005). The samples analyzed by Chatterjee et al. (2005) were collected from the Kolekole cinder cone, near the emergence of the volcano's southwest rift zone from the summit area. The near-vent scoria deposits and lava flows are mapped as Qhnv, with eruption age at 50–140 ka (Sherrod et al. 2006). Other samples containing clinopyroxene from the postshield Kula and Hana series with which we compare the new analyses were collected from drill core on the east flank of the volcano (Chen et al. 1990) and the inner wall of the volcano's summit crater (Fodor et al. 1975; Macdonald and Powers 1968).

X-ray fluorescence analysis

For each lava sample, two separate rock powders were prepared: one for the whole-rock (hereafter "WR") analysis and one for groundmass ("GM") analysis. The rocks were

first crushed into millimeter-sized chips in a tungsten-carbide (WC) plate mill (jaw crusher). A hand magnet was used to separate groundmass-rich fraction, which contains late-crystallizing Fe–Ti oxides. Rock powders were obtained by crushing the WR and GM-rich fractions in an alumina swing mill. The compositions were determined with the Siemens 303AS X-ray fluorescence (XRF) spectrometer of the University of Hawaii—Manoa (USA) using a Rh target, end-window X-ray tube. Major elements were analyzed on fused disks following methods in Norrish and Hutton (1969); trace elements were analyzed on pressed powder pellets with peak intensities corrected for backgrounds, line interferences, and absorption using methods similar to those of Chappell (1992). Corrected intensities were calibrated against a wide range of international rock standards. BHVO-1, UH-1 and W-2 were run as unknowns along with the samples of this study. Accuracy and precision data for this system are <1 % for SiO_2, TiO_2, Fe_2O_3, CaO and K_2O, 1–2 % for Al_2O_3, MnO, MgO and P_2O_5, and 5–10 % for Na_2O (Sinton et al. 2005).

Electron probe microanalysis (EPMA)

The chemical compositions of mineral phases were determined using the JEOL Hyperprobe JXA-8500F electron microprobe of the University of Hawaii—Manoa (USA). Analysis occurred over five sessions, differing slightly in analytical parameters as we sought to optimize the procedure. The beam was tuned at 15–20 kV and 15–20 nA, defocused to a 10 μm spot size. Na was analyzed first to minimize alkali loss. Five diffracting crystals were used at the same time among one LiFH (for Cr, Ni and eventually Ti), one LiF (for Fe, Mn and eventually Ti), one PETH (for K, Ca and P), one PETJ (for Ca and eventually Ti) and two TAPs (for Mg, Al, Na and Si). The standards used were Verma Garnet (for Mn), Kakanui Augite USNM 122142 (for Al, Fe, Si, Mg and Ca), Sphene glass (for Ti), Chromite USNM 117075 (for Cr), Amelia Albite (for Na), Orthoclase OR-1 (for K), Fluor-apatite USNM 104021 (for P), and NiO or Olivine San Carlos Fo90 USNM 111312/444 (for Ni). The counting time was 20–35 s for Fe and Cr, 20–40 s for Si, Al, Mg and Na, 20–45 s for Ca, 20–50 s for Ni, 25 s for K, 30–40 s for Ti, 30–55 s for Mn, and 60 s for P. Detection limit is in the range 0.01–0.015 wt% for Mg, Al, Na, Ca and Si, and 0.015–0.04 wt% for Cr, Fe, Ti, P and K. Analytical uncertainty (1σ) is <5 % for major elements, 5–50 % for minor elements and 50–100 % for trace elements.

Phase mode determination

Phase abundances were determined for polished thin sections of the same two samples for which whole-rock and EPMA analyses are reported. For each standard-size thin section, the mode was obtained by point counting a minimum 500 grid intersections on digital mosaics of plane polarized and cross-polarized light images. Volume abundances were converted to mass fractions using the densities of minerals and basalt glass for the groundmass computed for Ka01-GM using the method of Lange and Carmichael (1990).

Representative analyses spanning the full range in compositional variation were selected for mass balance calculations of mineral modes. The phases included the mean GM compositions obtained by replicate XRF analysis of each sample (Table 1), four pyroxenes determined to be representative based on calibrated X-ray element maps (as described below), three olivines (82-08-02; 81-08; 90-09-10; Table 2), and two spinels (RP-Spin1; S2-Spin1b from Chatterjee et al. 2005). The modal abundance of each phase was determined by solving the system of linear equations, $Ax = B$, where x contains the phase mode, A is the matrix of phase composition (i.e., mineral and GM compositions as oxide wt%), and B contains the whole-rock compositions.

Possible liquids with which phenocrysts equilibrated

The highly crystalline groundmass precludes determination of a liquid composition by EPMA analysis relevant to the interiors of clinopyroxene phenocrysts. The mechanically separated groundmass fractions constitute potential liquids with which phenocrysts might have equilibrated, and their compositions are determined by XRF, as described above. For each the Ka01 and Ka02 WR and GM compositions, the mode obtained by mass balance includes one olivine and one or two pyroxenes. Spinel is either not required for mass balance (Ka01) or is present in low abundance <1 wt% (Ka02). Although the calculations yielded slightly different ratios of pyroxene and olivine, the Mg-rich Al-poor pyroxene and the least magnesian olivine dominated the calculated modes for both Ka01 and Ka02. However, the modes are not sensitive to specific choices of pyroxene and olivine; modulating the clinopyroxene compositions available for the mass balance from among the analysis values yielded similar modal abundances and RSS values, so long as at least one pyroxene and one olivine were included.

The abundances of clinopyroxene and olivine required by mass balance calculations are much lower—30 and 21 wt%, respectively, for Ka01 and Ka02, than the crystallinities obtained from point counting (55–57 wt%; Table 2). The most plausible explanation of this discrepancy is that the GM separates contained phenocrysts fragments in addition to crushed groundmass. Although the GM compositions are not likely to represent liquids with which olivine and pyroxene phenocrysts equilibrated, they do provide constraints on the mass balance calculations, as control points on the trajectories of mineral subtraction lines linking the WR compositions to plausible liquids.

Table 1 Whole rock, groundmass, and calculated liquid compositions

Sample Type	XRF analyses				Calc	Calculated L_{array} compositions representing mineral subtraction in ϕ increments of 5 wt%										
	Ka01	Ka01	Ka01	Ka01	Ka01	Sample Ka01 utilizes cpx-rl. cpx-nm and ol-Fo_{79} in the proportions: pyx/ol = 1.8. sp/ol = 0 (i.e., no spinel)										
	WR[1]	GM[1]	WR-n[1]	GM-n[1]	WR(n)[4]	$\phi = 5$ wt%	10	15	20	25	30 (~GM)	35	40	45	50	55
SiO_2	43.48	43.34	44.22	44.26	44.15	44.22	44.22	44.23	44.24	44.24	44.25	44.26	44.27	44.28	44.30	44.32
TiO_2	2.43	2.95	2.47	3.01	2.48	2.54	2.62	2.70	2.80	2.91	3.03	3.18	3.35	3.55	3.79	4.08
Al_2O_3	10.94	13.38	11.13	13.66	11.12	11.44	11.79	12.18	12.61	13.11	13.67	14.33	15.09	15.99	17.07	18.39
FeOt	13.07	13.23	13.29	13.51	13.25	13.33	13.37	13.43	13.48	13.55	13.62	13.71	13.81	13.92	14.06	14.24
MnO	0.17	0.18	0.17	0.18	0.19	0.17	0.17	0.17	0.16	0.16	0.16	0.16	0.15	0.15	0.14	0.14
MgO	13.03	8.86	13.25	9.04	13.25	12.73	12.16	11.53	10.81	9.99	9.06	7.99	6.74	5.26	3.48	1.31
CaO	12.33	11.94	12.54	12.19	12.53	12.50	12.45	12.39	12.33	12.26	12.18	12.09	11.99	11.86	11.71	11.52
Na_2O	1.79	2.54	1.82	2.59	1.94	1.89	1.98	2.07	2.17	2.29	2.42	2.57	2.75	2.96	3.22	3.53
K_2O	0.77	1.08	0.78	1.10	0.77	0.82	0.87	0.92	0.97	1.04	1.11	1.20	1.30	1.42	1.56	1.73
P_2O_5	0.33	0.47	0.34	0.47	0.33	0.36	0.38	0.40	0.42	0.45	0.48	0.52	0.56	0.61	0.67	0.74
total	98.33	97.93	100	100	100	100	100	100	100	100	100	100	100	100	100	100
RSS					0.020						0.044					
Sample	Ka02	Ka02	Ka02	Ka02	Ka02	Sample Ka02 utilizes cpx-sd, ol-Fo_{76}, and sp-timt in the proportions: pyx/ol = 1.8, sp/ol = 0.074										
Type	WR[1]	GM[1]	WR-n[1]	GM-n[1]	WR(n)[4]	$\phi = 5$ wt%	10	15	21 (~GM)	25	30	35	40	45	50	55
SiO_2	42.65	42.64	43.79	43.81	43.80	43.79	43.80	43.80	43.81	43.81	43.82	43.83	43.84	43.85	43.86	43.88
TiO_2	2.45	2.81	2.52	2.89	2.54	2.58	2.65	2.73	2.85	2.92	3.04	3.17	3.33	3.51	3.73	4.00
Al_2O_3	11.00	12.79	11.29	13.14	11.34	11.65	12.05	12.49	13.15	13.56	14.21	14.96	15.84	16.87	18.11	19.62
FeOt	13.22	13.48	13.57	13.85	13.54	13.63	13.70	13.78	13.90	13.97	14.09	14.22	14.38	14.56	14.78	15.05
MnO	0.17	0.18	0.17	0.18	0.18	0.17	0.17	0.17	0.17	0.18	0.18	0.18	0.18	0.18	0.19	0.19
MgO	12.80	10.05	13.14	10.33	13.16	12.58	11.95	11.25	10.22	9.57	8.55	7.37	6.00	4.38	2.43	0.05
CaO	12.14	11.74	12.46	12.06	12.45	12.39	12.32	12.23	12.11	12.03	11.91	11.77	11.60	11.41	11.17	10.89
Na_2O	1.86	2.22	1.91	2.28	1.85	1.99	2.08	2.18	2.33	2.42	2.56	2.73	2.93	3.16	3.43	3.77
K_2O	0.78	0.99	0.80	1.02	0.79	0.84	0.89	0.94	1.02	1.07	1.14	1.23	1.33	1.45	1.60	1.78
P_2O_5	0.35	0.45	0.35	0.46	0.36	0.37	0.39	0.41	0.44	0.47	0.50	0.54	0.58	0.63	0.70	0.77
total	97.40	97.33	100	100	100	100	100	100	100	100	100	100	100	100	100	100
RSS					0.094				0.139							

[1] WR and GM compositions are averages of two replicate XRF analyses; Fe_2O_3 converted to FeOt for clarity of comparison. WR(n) and GM(n) are the normalized equivalents

[2] L_{array} compositions at the crystallinities indicated by point counts (Table 2), at ϕ ~ 30 and ϕ ~ 21.4 are similar to Ka01GM and Ka02GM, respectively. RSS values reflect this comparison

[3] L_{array} values at $\phi = 55$ represent the compositions corresponding to subtraction of minerals in the abundances observed in point counts (Table 2)

[4] WR(m) are calculated using the phase modes obtained by linear least-squares mass balance calculations, and compared against the WR-n values to compute the residual sum of squares (RSS) statistic

Arrays of relevant liquids that would be formed by progressive removal of an assemblage of olivine, pyroxene, and spinel from the Ka01 and Ka02 whole rocks are calculated by algebraically rearranging the mass balance equations to solve for the liquid phase composition. Two arrays of compositions representing subtraction of the minerals in the compositions and proportions employed in the mass balance calculations, Ka01_L_{array} and Ka02_L_{array}, are computed at increments of 5 wt% crystals subtracted from the WR compositions over the range of 5–55 wt% crystals. L_{array} compositions corresponding to Fe–Mg exchange equilibrium between observed pyroxene and olivine are shown in italicized text in Fig. 4a.

Clinopyroxene-liquid thermobarometry

Thermobarometric calculations were performed on clinopyroxene-liquid pairs using the algorithms included in the

Table 2 Modal analysis of Ka01 and Ka02

	Ka01	Ka02
Phase modes obtained by petrographic point count analysis		
n	588	543
Volume basis	vol%	vol%
Groundmass	46.6	43.6
Pyroxene	31.1	36.5
Olivine	17.2	13.4
Voids in groundmass	2.0	3.3
Voids in pyroxene	2.6	2.8
Voids in olivine	0.2	0.0
Opaques	0.3	0.4
Total	100.0	100.0
Mass basis (void-free)[2]	wt%	wt%
Groundmass	44.7	42.5
Pyroxene	35.3	41.6
Olivine	19.6	15.4
Spinel	0.4	0.5
Total	100.0	100.0
Crystallinity (wt%)	55.3	57.5
Pyx/ol[1]	1.8	2.7
Phase modes computed by linear mass balance[3]		
Groundmass (GM separate)	70.1	78.6
Pyroxene (rl + nm + sd)	19.0	13.5
Olivine (Fo_{76} + Fo_{79})	10.9	7.2
Spinel (timt)	0.0	0.6
Total	100.0	100.0
RSS	0.015	0.004
Crystallinity (wt%)	29.9	21.4
Pyx/ol	1.7	1.9

[1] The Ka02 point count contains several very large pyroxenes, giving rise to its high pyx/ol ratio. The point count from this section is not considered representative of the lava

[2] Volume percents converted to weight percents using mineral and densities estimated for Ka01GM and Ka02GM assuming they are glasses

[3] The Fo_{82} olivine and Mg-hercynite spinel were not required for mass balance of either sample

supplemental materials of Putirka (2008), which incorporate the pressure-independent thermometers of Putirka et al. (1996) and Nimis and Taylor (2000), the pressure-dependent thermometer of Putirka et al. (2003), and the temperature-independent barometers of Nimis (1995) and Nimis (1999). The calculations were performed using iterative determination of temperature and pressure for the interdependent thermometers and barometers, as coded in the supplemental materials accompanying Putirka (2008). The Fe–Mg exchange coefficient, K_D is calculated as $(Fe^{cpx}/Mg^{cpx})/[c(FeO^{liq}/MgO^{liq})]$, where concentrations are expressed on a molar basis with Fe^{2+}/Fe_{tot} in the liquid = 0.9 (Moore and Ault 1965). This value for c corresponds to oxygen fugacity conditions near 1.6 log units below the FMQ buffer for the compositions in Ka01_L_{array}, according to Kilinc et al. (1983).

In their study of rapidly grown clinopyroxene in synthetic Etna basalt, Mollo et al. (2010) evaluate the performance of this suite of equations for recovering experimental pressure, 500 MPa, in dynamic cooling experiments. For anhydrous conditions, the best barometers were Nimis (1995), followed by Nimis and Ulmer (1998), and Eq. 30 of Putirka (2008); for experiments with 1.3 wt% H_2O, the best barometers were Putirka et al. (2003) and Eq. 30 of Putirka (2008). The model pressures invariably increased with increasing cooling rate, which ranged from 0.5 to 15 °C min^{-1}. In the present case, cooling rate is unknown but potentially several orders of magnitude slower than the experimental rates utilized by Mollo et al. (2010). We base our selection of thermobarometers on the ability of models to recover experimental conditions of isothermal, isobaric phase equilibrium experiments of Putirka et al. (1996), spanning 800–3000 MPa and 1200–1475 °C. These runs utilize ankaramite from Mauna Kea's postshield stage as starting material, a material that is similar to the Haleakala samples. The thermometers and barometers were ranked by their ability to recover experimental conditions used by Putirka et al. (1996) over the full range in experimental pressure. The three most successful thermometers are, in order of decreasing accuracy, Putirka et al. (2003), Putirka (2008; Eq. 34) and Putirka et al. (1996; Eq. T1). However, the barometers of Putirka (2008) Eq. 32b, Eq. 30, and Eq. 32c most closely recover experimental pressure when solved iteratively using the (higher) temperature returned by the thermometer of Putirka et al. (1996; Eq. T2). In summary, according to this assessment, the best thermometer is the model of Putirka et al. (2003), and the best barometer is the clinopyroxene-only temperature-dependent barometer of Putirka (2008) Eq. 32b, with input temperature calculated using the model of Putirka et al. (1996).

We evaluate the accuracy of the selected combination of models by comparing the recovered experimental conditions for other experimental data sets involving clinopyroxene in basalt, performed from 0.2 to 3000 MPa and 1000–1475 °C (Baker and Eggler 1987; Bartels et al. 1991; Kinzler and Grove 1992; Putirka et al. 1996). The preferred thermometer (Putirka et al. 2003) yields temperatures averaging 11 °C above the experimental temperatures with a standard deviation of 43 °C. The selected barometer (Putirka 2008; Eq. 32b) utilizing temperature from Putirka et al. (1996) yields pressures averaging 60 MPa below the experimental pressures, with a standard deviation of 154 MPa (Fig. SM3).

Results

Petrography

Samples Ka01 and Ka02 are texturally similar, with ~50 vol% crystals and sparse vesicles set in a crystalline groundmass (Fig. 2; Table 2). Crystals include macrocrysts (0.5–30 mm diameter), mesocrysts (0.1–0.5 mm diameter), and microcrysts (<0.1 mm diameter). Macrocrysts and mesocrysts (together "phenocrysts" here) are exclusively olivine and clinopyroxene.

The textures of olivine macrocrysts are similar to those found in olivine-rich basalts (Helz 1987; Welsch et al. 2013) composed of crystallographically coherent polyhedral crystals units exhibiting occasional angular misorientations, twins, Cr-spinel inclusions, and cavities filled with melt and/or fluid (void space).

Clinopyroxene is the dominant phase in these size ranges and is characterized by the ubiquitous presence of spongy subgrain domains, typified by epoxy-filled spaces up to several hundred microns in diameter. Spongy domains are located within the interiors of some crystals and at the margins of others, precluding a consistent designation as either "core" or "rim." We interpret the angular boundaries of a great majority of void spaces to represent removal of matrix material during preparation of billets or during thin section preparation. However, given the delicate diktytaxitic texture within some cavities (Fig. 2d), we conclude that not all voids are artifacts of sample preparation (e.g., plucking). Additional petrographic data are given in Welsch et al. (2015).

With respect to birefringence and extinction angle, the distinction between spongy domains is barely perceptible. The textural duality of individual clinopyroxene crystals is so pervasive as to be a first-order characteristic distinguishing clinopyroxene from olivine, which lacks spongy-textured domains. A second-order feature is Z-contrast within textural domains. The outermost rims of clinopyroxene crystals represent a distinctive, spatially coherent domain typically $\leq$50 μm thick. These rims are evident in BSE images as anomalously bright pixels (high Z-contrast). These rims are laterally continuous, armoring the non-spongy and spongy domains alike from contact with matrix (Fig. 3).

Microcrysts are, in order of decreasing abundance, clinopyroxene, plagioclase, Fe–Ti-oxide and olivine. Mesocrysts and microcrysts are anhedral and are not considered further.

WR and GM compositions

The whole rock (WR) and mechanically separated groundmass (GM) compositions of Ka01, Ka02 as well as potential liquid compositions obtained by numerical mineral subtraction from the WR are presented in Table 1. Similar to the whole-rock analyses of Hana series ankaramites drilled on the east flank of Haleakala 65 (Chen et al. 1990), the whole rock and GM compositions of Ka01 and Ka02 plot in the picrobasalt and basanite fields in a total alkalis versus silica variation diagram (Fig. 4a). The WR compositions of Chatterjee et al. (2005) share similar ratios of Al_2O_3 to MgO (Fig. 4b), but differ from the Qkuls samples in extending to lower SiO_2 (Fig. 4a). The calculated matrix compositions of Chatterjee et al. (2005) extend to higher CaO concentrations and do not vary coherently with respect to MgO (Fig. 4c).

Mineral compositions

Olivine macrocrysts are spatially homogeneous in composition, with <1 mol % Fo variation within individual crystals. The overall range in composition among analyzed crystals is $Fo_{76.3}$ to $Fo_{82.4}$ (Table 3).

The letters "d", "m", or "l" associated with clinopyroxene analyses (Table 4) indicate whether the areas appear relatively dark, medium, or light in BSE imaging, with "s", "n", and "r" indicating spongy, non-spongy, or rim domain type (e.g., Fig. 3). Clinopyroxene macrocrysts span a relatively restricted range in major element concentrations (Fig. 5), corresponding to ternary compositions that extend from $En_{44.8}Fs_{10.1}Wo_{45.1}$ as the most magnesian crystal interior to $En_{35.1}Fs_{15.3}Wo_{49.6}$ at the most ferroan outermost rim. Clinopyroxene analyses from crystals in the Ka01 and Ka02 thin sections are classified dominantly as aluminian chromian (±ferrian) subsilicic diopside according to Sturm (2002), following the criteria of Morimoto et al. (1988) and computing Fe^{3+} following the method of Lindsley (1983). A loose crystal weathering from the same Qkuls flow, aug3 (Fig. SM2), contains the greatest MgO and SiO_2 (and correspondingly the least Al_2O_3, TiO_2, and CaO) in the data set, and these pyroxene compositions are classified as aluminous augite.

Despite the overall low variance among major element concentrations, individual crystals span a relatively wide range of nonstoichiometric element concentrations (Table 4; selected variation diagrams in Fig. 5). For example, the range in TiO_2 contents spanned by the seven crystals analyzed in this study (3.6 wt%) constitutes 90 % of the maximum observed TiO_2 concentration (4.3 wt%). Typically, MgO-rich analyses are higher in SiO_2 and Cr_2O_3; Al^{iv} and TiO_2 are inversely correlated with MgO (Fig. 5). As the non-spongy and spongy subgrain textural domains span identical ranges and exhibit identical covariations, no correspondence of composition with textural type is resolvable from the spot EMP data. In contrast, for a given MgO content, the outermost crystal rims are consistently lower in Na_2O and SiO_2 and elevated with respect to CaO, FeO,

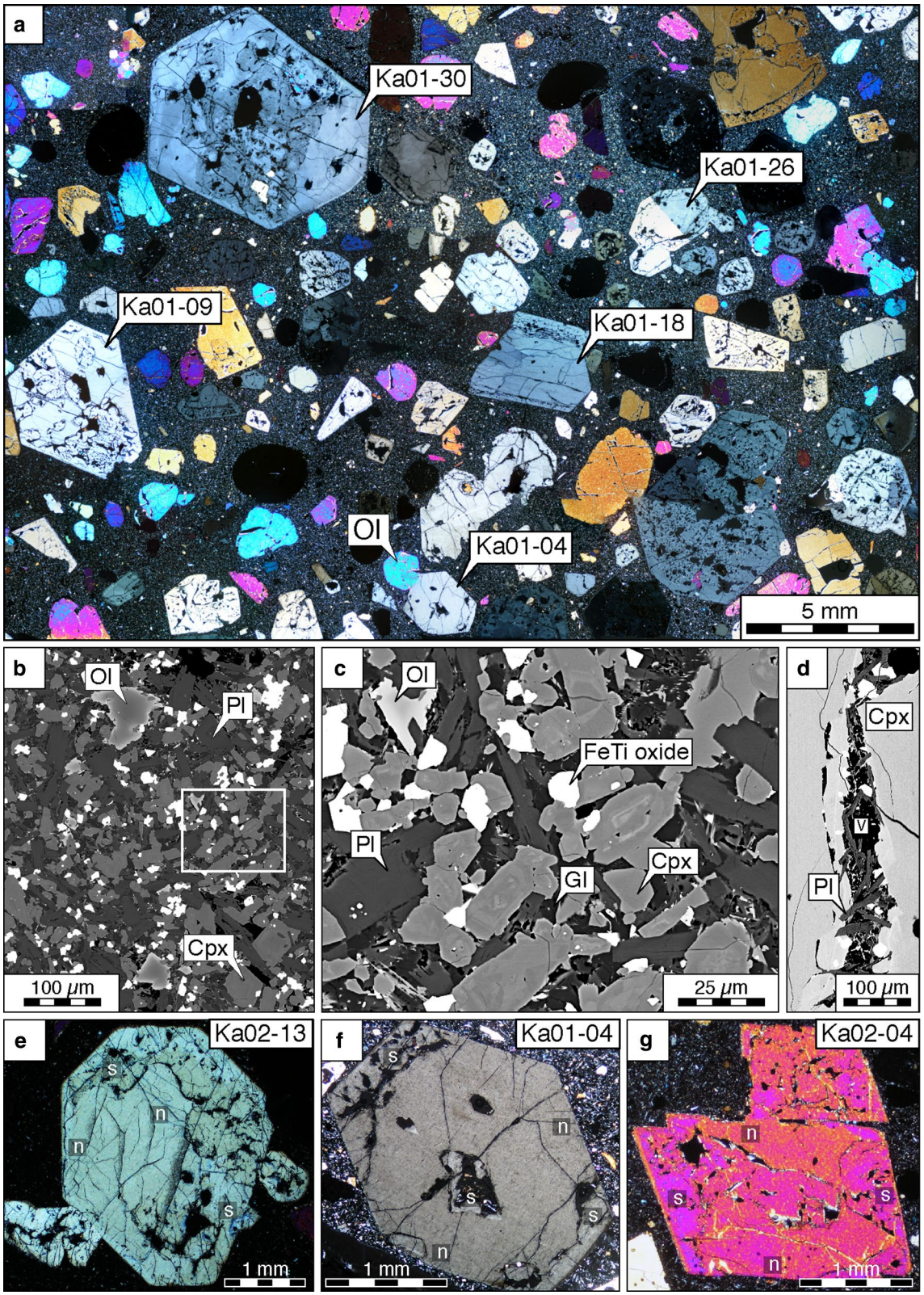

Fig. 2 Representative regions of thin sections Ka01 and Ka02 from Qkuls ankaramite. **a** Cross-polarized light (XP) panorama of nearly the entire Ka01 thin section. **b** Back-scattered electron image of Ka01 groundmass, with inset box expanded in **c** to reveal plagioclase laths (Pl), zoned clinopyroxene (Cpx) and olivine (Ol) microcrysts, and pockets of glass (Gl). **d** Detail of spongy domain inside a clinopyroxene crystal showing diktytaxitic texture (delicate plagioclase crystals protruding into void space). **e**–**g** XP views of crystals in Ka01 and Ka02, with non-spongy (n) and spongy (s) domains occurring at crystal interiors as well as within faceted margins

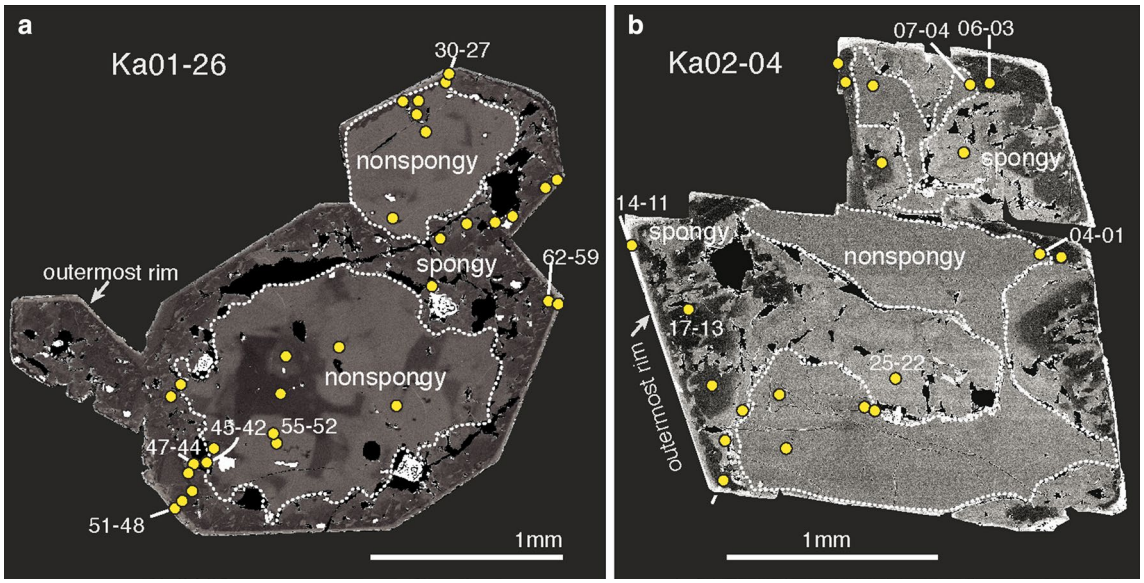

Fig. 3 Back-scattered electron images of selected crystals described in the text. The matrix has been masked, and the dark background enhances the outermost rims, which are brighter than interior regions. A *dotted white line* enhances the boundary between spongy and non-spongy domains. The locations of EMP-WDS analyses are as indicated with *yellow dots* and labeled with analysis numbers corresponding to the entries in Table 4. *Yellow dots* are ~20 × larger than EMP spot sizes

TiO_2, and Al_2O_3 as compared with analyses from the crystal interiors.

The compositions of three individual crystals selected as representative of the Qkuls clinopyroxene that are the particular focus of this study, Ka01-26, Ka01-18, and Ka02-04, are not only similar to each other, but also span a range in composition that is similar to clinopyroxenes from other alkali-rich magmas from Haleakala (Chatterjee et al. 2005; Chen et al. 1990; Fodor et al. 1975). Clinopyroxene compositions reported by Fodor et al. (1975) for alkalic magmas are averages of 100 microprobe spots. The elemental covariations among all these ankaramite clinopyroxene data sets are also similar. The only notable difference between the Qkuls clinopyroxene macrocrysts from the ankaramite lava flow and those of the Kolekole cone (Chatterjee et al. 2005) is the slightly higher maximum MgO of the ankaramite flow crystals and lower minimum abundances of Al, Ti, and Na in the Kolekole crystals.

X-ray element maps

The WDS analyses obtained by EPMA are used to establish quantitative correlations between Na and Al k_α X-ray counts and metal oxide abundances in weight percent for selected crystals. (A similar procedure is developed by Lanari et al. 2014). Figure 6 shows the calibration procedure applied to Ka02-04, as well as the corresponding element variation diagrams as two-dimensional (2D) frequency histograms. The calibration procedure leverages the ~30 analyses per crystal to quantitatively relate the more than 10,000 pixels intensity values within each textural domain to the corresponding metal oxide abundance. This step permits critical examination of key inferences: (1) that several dozen spots selected with the intention of capturing the full compositional range of a given crystal can be spatially representative and (2) that the spongy and non-spongy textural domains evident in PL and BSE images are compositionally indistinguishable, as suggested by the spot analyses (Fig. 5). With regard to the first inference, the most frequently occurring compositions (bounded by dotted lines in Fig. 6) revealed by the maps are within the ranges sampled by the spot analyses. However, the mode of the distribution (arbitrarily enclosing red-hued frequencies in the color scale) is not manifest as a cluster of points in the array of spot analyses (Fig. 4). The frequency histograms further reveal a subtle distinction between spongy and non-spongy domains: the median concentration of Al_2O_3 in the non-spongy domains is 1.16 wt% (16 % relative) higher than in the spongy domains; mean Na_2O in the non-spongy domains is 0.14 wt% (26 % relative) higher than in the spongy domains. Conventional histograms depicting the frequency distributions of this oxide wt% along with the median and standard deviation values are included in Fig. SM4.

Clinopyroxene-liquid thermobarometry applied to spot analysis

The full spectrum of results from the preferred combination of thermometer and barometer applied to analytical spots

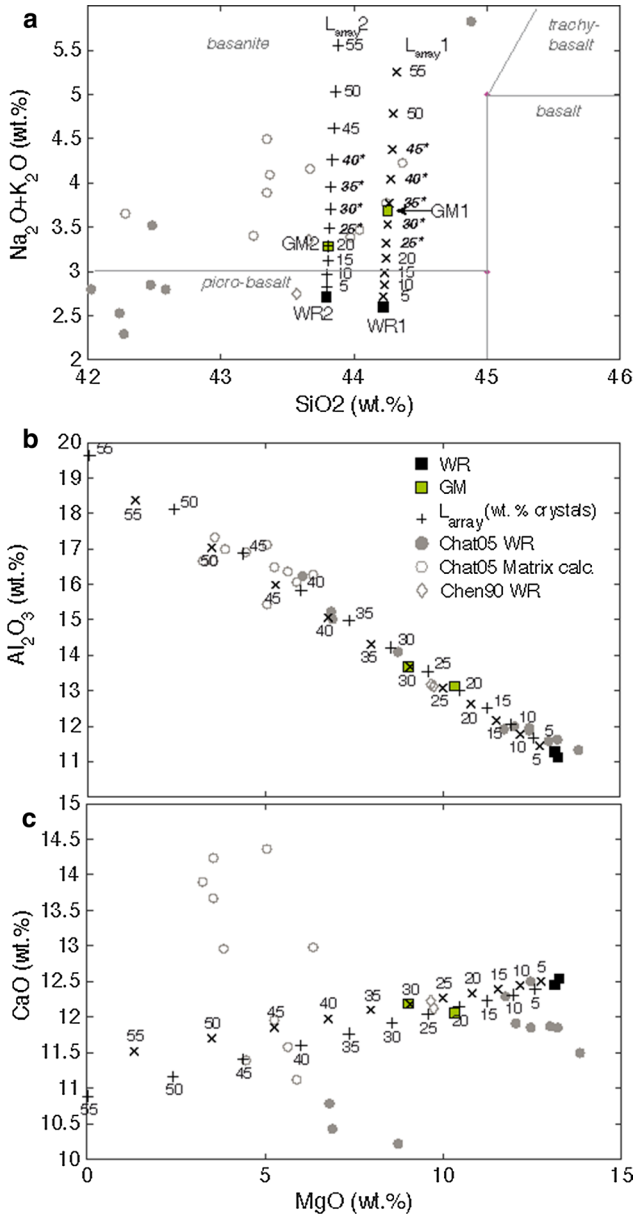

Fig. 4 Major element variation diagrams for Ka01 and Ka02 whole rocks (WR), mechanically-separated matrix fractions (GM), and potential matrix liquids calculated by subtracting minerals in the proportions and compositions observed in the Ka01 thin section of QKuls ankaramite. The L_{array} compositions pass through GM and values because the proportions of minerals observed in thin section are similar to those satisfying mass balance. The L_{array} compositions satisfying Fe–Mg exchange equilibrium with the analyzed clinopyroxenes in each sample are indicated with *bold*, italicized labels with *asterisks* in **a**. The WR and estimated liquid compositions reported for Kolekole scoria (Chatterjee et al. 2005) and Hana series ankaramite (Chen et al. 1990) are shown as *solid circles*, *open circles*, and *open diamonds*, respectively. See text for more details

within Ka01-18, Ka01-26, and Ka02-04, satisfying temperature-dependent Fe–Mg exchange equilibrium (according to the algorithm of Putirka (2008)) with compositions computed along the Ka01-L_{array} or Ka02-L_{array}, is shown in Fig. 7. The number of points plotted exceeds the number of clinopyroxene analyses because several analyses satisfy Fe–Mg exchange equilibrium with more than one L_{array} composition, and in these cases, all solutions are depicted. The pairings that yield the closest match between observed and predicted clinopyroxene components (DiHd, EnFs, CaTs, etc., as formulated in Putirka 1999) also typically yield the lowest pressure. A representative subset of pairs is presented in Table 5, along with pressure and temperature values calculated using other algorithm combinations.

The calculated pressures are correlated with calculated temperatures as well as the amount of crystal subtraction along the L_{array} required to satisfy Fe–Mg exchange equilibrium. The values are lowest (1160–1180 °C and <400 MPa) in the pairings of outermost rims with the most evolved L_{array} compositions, i.e., those representing subtraction of 40–45 wt% crystals from the respective WR compositions. The values are highest (1290 °C and 900 MPa) in clinopyroxene analyses paired with L_{array} compositions representing as little as 25 wt% crystal subtraction from the WR. Intermediate values of temperature and pressure are correspondingly obtained from pairings with L_{array} compositions representing 30–35 wt% crystal subtraction. These correlations arise from the dependence of calculated temperature on the Mg contents of clinopyroxene and liquid, the dependence of calculated pressure on Na contents of clinopyroxene, and the generally compatible behavior of Na in these crystals. Interestingly, the correlation between Al_2O_3 and calculated pressure typical of clinopyroxene-bearing phase equilibrium experiments is not evident in the ankaramite data set (Fig. SM5); instead, the calculated pressure is weakly inversely correlated with the Al content of natural clinopyroxene.

Olivine-liquid thermometry was applied to the two analyses used in mass balance calculations (Ka01-82-08-02 and Ka01-90-09-10; Table 3) and the computed liquids with which they are in Fe–Mg exchange equilibrium corresponding to 32.5 and 20 wt% crystals removed, respectively. Crystal 82-02, paired with L_{array} compositions, representing 30–35 wt% crystal subtraction yields 1207–1226 °C using the thermometers of Beattie (1993) and Putirka (2008). Crystal 90-09-10, paired with the L_{array} composition, representing 20 wt% crystal subtraction (slightly more mafic than the most magnesian liquid required by cpx-liquid Fe–Mg exchange equilibrium) is 1270–1274 °C. These temperatures are coincident with the high to intermediate range retrieved by clinopyroxene-based thermometry.

The calculated pressures and temperatures are lowest for analyses from the outermost crystal rims, as predicted from the low-Na contents of these spots (Fig. 5d, e). Also consistent with the lack of apparent correlation between the spongy/non-spongy textural distinction and

Table 3 Representative olivine analyses

Sample analysis	Ka01 7	Ka01 81-08[2]	Ka01 9	Ka01 10	Ka01 12	Ka01 7b	Ka01 82-08-02[2]	Ka01 90-09-10[2]	Ka01 9b	Ka01 10b	Ka01 12b
SiO_2	37.9	37.8	37.9	38.1	38.0	38.4	38.1	38.4	38.6	38.3	38.0
TiO_2	0.03	0.03	0.03	0.00	0.01	0.02	0.02	0.01	0.00	0.03	0.03
FeO	21.99	22.18	20.95	20.68	21.82	19.29	19.85	16.68	18.24	18.72	21.69
MnO	0.27	0.32	0.32	0.25	0.33	0.23	0.27	0.20	0.23	0.27	0.35
MgO	40.74	40.18	41.38	41.51	40.22	42.70	41.64	43.73	43.24	42.36	40.52
CaO	0.22	0.21	0.21	0.22	0.23	0.27	0.37	0.32	0.32	0.34	0.21
NiO	0.15	0.12	0.15	0.17	0.14	0.18	0.17	0.20	0.19	0.17	0.11
Total	101.3	100.9	101.0	101.0	100.8	101.2	100.5	99.7	100.9	100.3	101.0
Fo	76.8	76.3	77.9	78.1	76.7	79.8	78.9	82.4	80.9	80.1	76.9
L_{array} (ϕ)[1]	37.5	37.5	35.0	35.0	37.5	30.0	32.5	20.0	27.5	30.0	37.5

[1] The composition along Ka01-Larray in Fe–Mg exchange equilibrium with the given olivine, expressed as the crystal content (ϕ) removed from WR

[2] Analysis is used in mass balance calculations

elemental abundances (Fig. 5a–c) is a lack of correlation between texture type and calculated temperature and pressure. Spongy and non-spongy domain types appear to span indistinguishable ranges and are evenly distributed across P–T space. Moreover, the breadth of values spanned by individual crystals is similar to the intracrystalline range, mirroring the distribution of elemental abundances (Fig. 5).

Uncertainty in the liquid compositions (arising from lack of glassy samples) is an important weakness in this application of thermobarometry. (The sensitivity to liquid composition in the pressures calculated from Putirka (2008) Eq. 32b, a clinopyroxene-only barometer, arises through its influence on calculated temperature from the Putirka et al. (1996) thermometer.) Random pairings of the observed clinopyroxene compositions with unrelated liquids (satisfying Fe–Mg equilibrium) indicates the observed variation in Na contents within the ankaramite crystals is sufficient to generate a range in pressure of up to 300 MPa. The full range of observed pressure variation (nearly 1000 MPa) is only generated through pairings of clinopyroxene with reasonable liquids; our calculated mineral subtraction arrays represent a plausible approach to determining reasonable liquid compositions.

The approach taken by Chatterjee et al. (2005) also involves subtraction of minerals from whole-rock compositions, but instead of locating points along a subtraction line that satisfy Fe–Mg equilibrium, phases are subtracted in the abundances in which they are observed. The crystallinities of our samples are ~50 vol%. Subtraction of olivine and clinopyroxene in the observed proportion and abundance (Table 2) yielded compositions too poor in Mg to satisfy Fe–Mg equilibrium with any clinopyroxene analysis and point toward substantial crystal accumulation.

Given the similarity in samples and approach, it is instructive to compare our results with those of Chatterjee et al. (2005) for Kolekole scoria. We calculate equilibrium pressure and temperature using their published phase compositions. This produces a range of pressure values that is similar to our determinations for the ankaramite lava (Fig. 7). The Chatterjee et al. (2005) temperatures are much lower ($\leq$1210 °C), presumably owing to the lower Mg contents of the computed liquids. However, the range of pressure preferred by Chatterjee et al. (2005) extends higher than the values we obtain and do not overlap the pressure values we obtain for rims. The maximum rim pressure value of Chatterjee et al. (2005) is 1120 MPa, which is >900 MPa greater than highest pressure obtained from outermost rims in our study (170 MPa) with the preferred thermometer–barometer combination. The difference cannot be attributed to the choice of liquid or clinopyroxene compositions but rather is a consequence of their selection of the Putirka et al. (1996) barometer. As a confirmation, we applied the Putirka et al. (1996) barometer to the clinopyroxene-liquid pairs of Chatterjee et al. (2005) and calculated values that closely approach their maximum value (1200 MPa), and importantly, yields values 400–700 MPa higher than the corresponding results from our selected barometer (Putirka 2008; Eqn. 32b, utilizing temperature from Putirka et al. 1996).

Clinopyroxene-liquid thermobarometry applied to element maps

Thermobarometry is predicated on the difference in molar volumes of various components that substitute for stoichiometric clinopyroxene components, and the resultant tendency for element substitutions to minimize molar volume

Table 4 Representative clinopyroxene analyses

Crystal	Ka_02-04	Ka_02-04	Ka_02-04	Ka_02-04	Ka_02-04	Ka_02-04	Ka_02-04	Ka_01-26	Ka_01-26
Analysis	14-11	17-13	07-04	06-03	09-06[4]	25-22	04-01	51-48	30-27[4]
Type[1]	rl	sd	sl	nd	nm	nm	nl	rl	rl
SiO_2	43.6	50.0	48.2	50.1	45.7	47.4	48.3	45.2	46.2
TiO_2	4.29	1.26	1.76	1.21	2.10	1.96	1.89	3.21	2.92
Al_2O_3	10.31	6.15	8.21	6.40	8.05	7.71	8.48	8.98	8.48
FeO	8.58	5.87	7.24	6.01	7.02	7.12	7.22	8.20	7.92
MnO	0.11	0.10	0.10	0.10	0.05	0.10	0.12	0.09	0.13
MgO	11.19	15.05	13.38	14.73	13.54	13.60	13.53	12.31	12.81
CaO	21.96	21.39	20.20	20.93	21.92	22.03	20.15	22.81	22.47
K_2O	0.01	N.A.	N.A.	0.00	N.A.	0.02	0.01	0.02	0.02
Na_2O	0.51	0.60	0.70	0.66	0.53	0.57	0.78	0.41	0.46
NiO	0.02	0.05	0.01	0.02	0.03	0.02	0.02	0.05	0.03
Cr_2O_3	0.08	0.49	0.31	0.91	0.44	0.30	0.32	0.06	0.11
Total	100.6	101.0	100.1	101.1	99.4	100.9	100.8	101.3	101.5
Name[2]	Aluminian ferrian subsilicic titanian	Aluminian chromian	Aluminian	Aluminian chromian	Aluminian chromian ferrian subsilicic	Aluminian ferrian subsilicic	Aluminian	Aluminian ferrian subsilicic	Aluminian ferrian subsilicic
	Diopside	Diopside	Diopside	Diopside	Diopside	Diopside	Diopside	Diopside	Diopside
En	35.13	44.56	41.78	44.38	42.06	40.62	42.11	36.90	38.26
Fs	15.31	9.92	12.87	10.33	12.61	12.09	12.82	13.95	13.49
Wo	49.56	45.52	45.35	45.29	45.32	47.29	45.07	49.15	48.25
Mg#[3]	78.9	87.8	79.6	84.8	90.2	88.2	80.9	85.6	85.3
Crystal	Ka_01-26	Ka_01-26	Ka_01-26	Ka_01-26	Augite 3	Augite 3	Augite 3	Augite 3	Augite 3
Analysis	47-44[4]	62-59	45-42	55-52	06-02	68-65	08-32	spot 07	07-32
Type[1]	sd	sd	sl	nd	rl	sd	nd	nm	nl
SiO_2	48.8	49.2	47.2	47.4	44.9	46.7	50.6	47.8	45.8
TiO_2	1.32	1.26	1.94	1.74	3.20	2.16	0.82	1.87	2.27
Al_2O_3	6.82	6.26	7.54	8.24	9.06	8.79	6.21	7.96	8.76
FeO	5.95	5.81	6.89	6.90	8.04	7.60	6.74	7.18	7.68
MnO	0.07	0.10	0.12	0.12	0.09	0.09	0.13	0.12	0.10
MgO	14.81	14.98	13.71	13.96	12.13	13.37	15.54	13.62	12.81
CaO	21.77	21.84	22.01	21.32	22.50	21.34	19.95	21.38	21.14
K_2O	0.00	0.01	0.01	N.A.	N.A.	N.A.	N.A.	0.01	N.A.
Na_2O	0.62	0.67	0.60	0.65	0.45	0.65	0.56	0.60	0.68
NiO	0.01	0.04	0.03	0.04	0.02	0.01	0.02	0.00	0.02
Cr_2O_3	0.86	0.87	0.45	0.46	0.05	0.12	0.03	0.30	0.14
total	101.0	101.1	100.5	100.9	100.4	100.9	100.6	100.8	99.4
Name[2]	Aluminian chromian ferrian	Aluminian chromian ferrian	Aluminian chromian ferrian subsilicic	Aluminian chromian ferrian subsilicic	Aluminian ferrian sub-silicic	Aluminian ferrian sub-silicic	Aluminian	Aluminian subsilicic	Aluminian ferrian subsilicic
	Diopside	Diopside	Diopside	Diopside	Diopside	Diopside	Augite	Diopside	Diopside
En	43.79	44.08	40.96	42.01	36.91	40.49	46.06	41.17	39.58

Table 4 continued

Crystal	Ka_01-26	Ka_01-26	Ka_01-26	Ka_01-26	Augite 3	Augite 3	Augite 3	Augite 3	Augite 3
Analysis	47-44[4]	62-59	45-42	55-52	06-02	68-65	08-32	spot 07	07-32
Type[1]	sd	sd	sl	nd	rl	sd	nd	nm	nl
Fs	9.97	9.76	11.75	11.87	13.89	13.06	11.44	12.38	13.50
Wo	46.24	46.17	47.29	46.13	49.20	46.44	42.50	46.45	46.93
Mg#[3]	92.0	92.8	90.5	89.6	84.7	87.0	84.2	85.2	86.3

[1] Textural type assessed during analysis using BSE imaging of sample. "rl" BSE-light outermost crystal rim; "sd" BSE-dark spongy region; "sl" BSE-light spongy region; "nm" BSE-medium non-spongy region; "nl" BSE-light non-spongy region

[2] Pyroxene name assessed using guidelines established nomenclature of pyroxenes (Morimoto et al. 1988)

[3] Mg# computed as $Mg/(Mg + Fe^{2+})*100$ on cation basis, following Sturm (2002) and Morimoto et al. (1988), with Fe speciation computed according to Lindsley (1983)

[4] Analysis is used in mass balance calculations

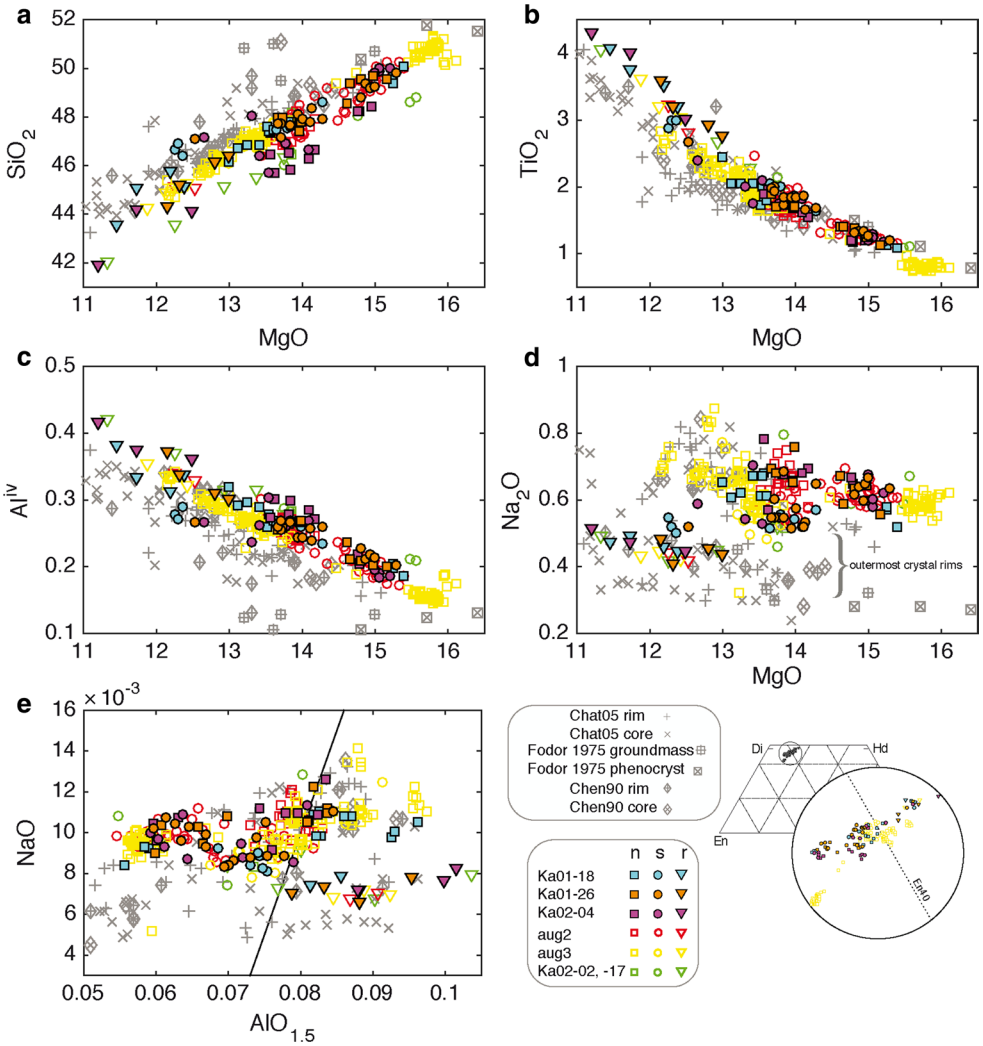

Fig. 5 Variation diagrams depicting EMP spot analytical data from seven crystals in the Qkuls samples, clinopyroxene in alkalic basalts of Fodor et al. (1975), the Hana and Kula lavas of Chen et al. (1990), and the Kolekole lavas of Chatterjee et al. (2005). Quadrilateral and circular inset depicts end-member pyroxene concentrations of all Qkuls analyses. *Symbol shape* and *color* indicate crystal and texture type, as defined in the legend. Note that the core and rim designations (multi and plus symbols, respectively) attributed to Kolekole analyses in Chatterjee et al. (2005) are not associated with the textural domains (spongy, non-spongy, outer rim) identified in the Qkuls ankaramite lava crystals. *Solid black line* in **e**. has slope = 1 (arbitrary intercept) and indicates the covariation trend consistent with simple jadeite substitution. The rim compositions span an array with positive slope that is distinct from this line, suggesting that other substitutions are also important

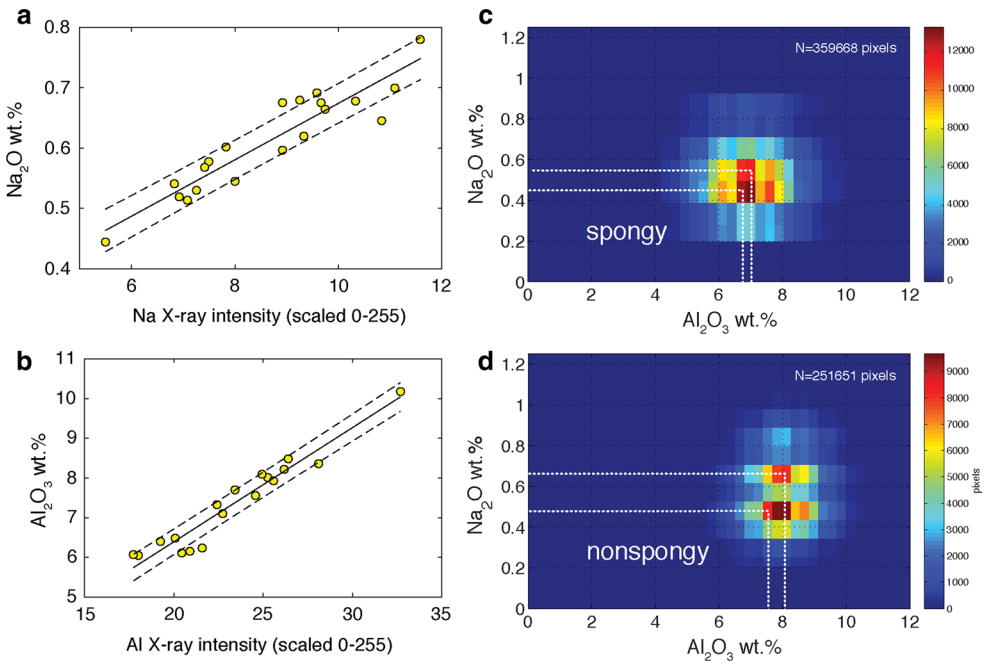

Fig. 6 Relationship between semi-quantitative element concentration data obtained from X-ray maps and quantitative spot analyses for crystal Ka02-04. **a**, **b** Concentrations plotted on the *y*-axis are obtained from WDS spot analyses of spongy, non-spongy, and outermost rim texture types (Fig. 3). The locations of spot analyses were marked on digital BSE images, and the corresponding X-ray intensity values from the nearest 9–12 pixels at each spot were averaged to obtain the values plotted on the *x*-axis. **c**, **d** "Cloudplots" show the frequency of concentrations for each texturally distinct region in clinopyroxene crystals. *Dotted white lines* guide the eye to the most frequently occurring ordinate and abscissa values. Similar plots for additional crystals and elements, as well as the outermost rims of Ka02-04, are included in Figure SM7

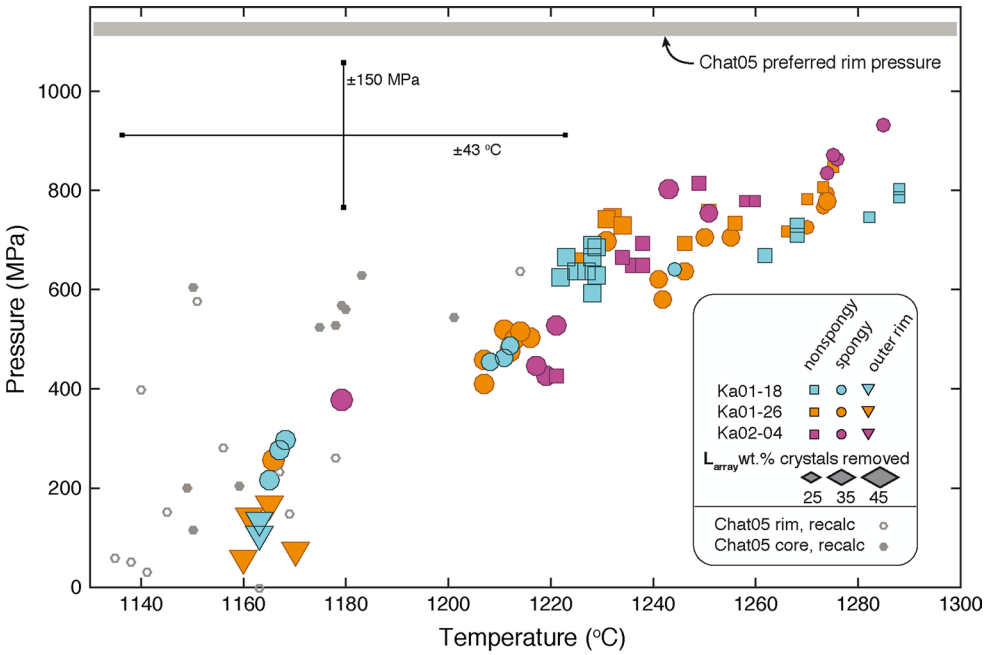

Fig. 7 Calculated pressures and temperatures using clinopyroxene-liquid pairs that satisfy Fe–Mg equilibrium for the three crystals indicated. *Black dots* indicate that the clinopyroxene and liquid compositions for these pairs are given in Table 5. *Symbol size* reflects the amount of crystals subtracted from the WR required to satisfy the Fe–Mg equilibrium constraint. The *error bars* are estimated by applying the thermobarometers to experimental data (see Fig. SM3). Calculated conditions for the clinopyroxene-liquid pairs from Chatterjee et al. (2005) using the same combination of thermobarometers are as shown in *small gray circles*. *The shaded horizontal bar* indicates the range of rim pressure values preferred by Chatterjee et al. (2005) using the barometer of Putirka et al. (1996)

Table 5 Geobarometry for representative clinopyroxene-melt pairs satisfying Fe–Mg equilibrium

cpx analysis	Liquid	K_D (Fe–Mg)[1]	K_D (Fe–Mg) Equation 35. Putirka (2008); T-dep't K_D	T (°C) Putirka et al. (2003)[2]	T (°C) Equation 34 Putirka (2008) after Putirka (1996)	P (MPa) Equation 30 Putirka (2008)	P (MPa) Equation 32a Putirka (2008) based on Nimis (1995)[3]	P (MPa) Equation 32b[4] Putirka (2008). based on Nimis (1995)[3]	P (MPa) Equation 32c Putirka (2008)[3]
Ka01-26 51-48	Ka01 L_{array} $\phi = 45$	0.28	0.27	1160	1193	528	555	60	1078
Ka01-26 52-49	Ka01 L_{array} $\phi = 45$	0.27	0.27	1166	1209	666	552	259	921
Ka01-26 43-40	Ka01 L_{array} $\phi = 40$	0.28	0.28	1214	1253	841	833	518	1185
Ka01-26 62-59	Ka01 L_{array} $\phi = 35$	0.29	0.29	1274	1323	1159	1039	779	1441
Ka01-26 57-54	Ka01 L_{array} $\phi = 30$	0.28	0.29	1266	1309	1033	942	719	1309
Ka01-26 58-55	Ka01 L_{array} $\phi = 40$	0.28	0.29	1234	1278	1084	1095	732	1348
Ka01-18 84-81	Ka01 L_{array} $\phi = 45$	0.27	0.27	1163	1199	583	585	108	1112
Ka01-18 78-75	Ka01 L_{array} $\phi = 45$	0.28	0.27	1165	1206	644	558	216	983
Ka01-18 70-67	Ka01 L_{array} $\phi = 25$	0.31	0.30	1288	1332	1137	1041	805	1456
Ka01-18 88-85	Ka01 L_{array} $\phi = 40$	0.31	0.28	1228	1267	988	1050	594	1478
Ka02-04 15-14	Ka02 L_{array} $\phi = 25$	0.30	0.30	1285	1334	1219	1198	935	1459
Ka02-04 23-20	Ka02 L_{array} $\phi = 40$	0.27	0.28	1179	1228	727	611	378	906
Ka02-04 25-22	Ka02 L_{array} $\phi = 35$	0.30	0.28	1221	1269	903	801	429	1406
Ka02-04 20-17	Ka02 L_{array} $\phi = 35$	0.30	0.29	1238	1284	1061	1067	649	1495
Ka02-04 06-03	Ka02 L_{array} $\phi = 30$	0.27	0.29	1260	1310	1123	1051	778	1368

[1] Calculated assuming liquid $Fe^{2+}/Fe_{total} = 0.9$

[2] This model best reproduces the experimental temperature at which phase equilibria experiments were performed on ankaramite (Putirka 1996)

[3] Temperature was calculated using Putirka (1996), Eq. T1

[4] This model best reproduces the experimental pressures at which phase equilibria experiments were performed on ankaramite (Putirka 1996)

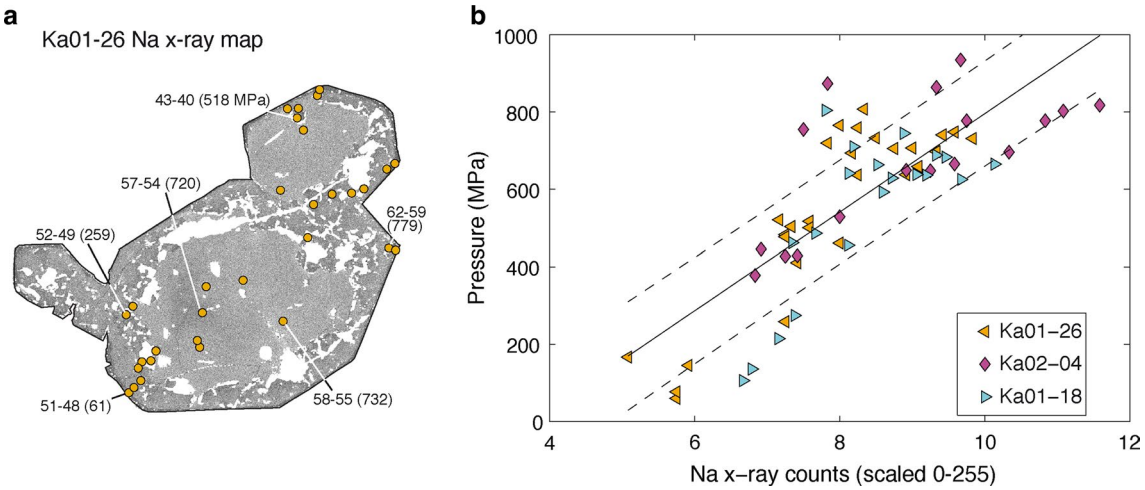

Fig. 8 Illustration of steps in recalibrating Na x-ray element maps as pressure maps. **a** Na x-ray map of crystal Ka01-26, masked to remove from consideration matrix and void pixels, shows locations of spots analyzed quantitatively using WDS-EPMA on Ka01-26. The equilibrium pressure represented by the compositions at these spots is calculated as described in the text. The analysis number and calculated pressure (in MPa) are as indicated for selected points. **b** The pressures obtained from Ka01-26 spots, combined with spots from Ka01-18 and Ka02-04, correlate with the abundance of Na X-ray counts in EMP element maps at the spot locations (located manually). Additional details provided in Figure SM6. The *solid line* is the linear least-squares best fit, with *dashed lines* estimating one standard deviation (enclosing 50 % of future values, assuming a normal distribution). The correlation, which is highly dependent upon mapping conditions and is therefore not transferable beyond this study, is then applied to each pixel in the Na X-ray maps (coded in MATLAB) to transform X-ray counts into pressure

as pressure increases. The jadeite exchange equilibrium, $NaO_{0.5}^{liq} + AlO_{1.5}^{liq} + 2SiO_2^{liq} = NaAl_2O_6^{cpx}$ possesses the largest ΔV of reaction, -23.5 cm^3 mol^{-1} of the common molecular substitutions in clinopyroxene (Putirka et al. 2003). Increasing pressure drives this reaction forward, increasing the equilibrium partitioning of Na and Al into sites normally occupied by Ca, Fe, Mg, and Si. Although clinopyroxene-liquid thermometers and barometers include terms parameterizing the abundances of other elements in both phases, we determined empirically using the Qkuls data set that the Na content of the clinopyroxene exerts the greatest influence on calculated pressure, consistent with previous observations (e.g., Kornprobst et al. 1981). We then exploited the observed linear relationships between oxide wt% and X-ray counts (Fig. 6 and SM6), and between Na X-ray counts and calculated pressure (Fig. 8), to convert the X-ray element maps of Welsch et al. (2015) into pressure maps (Fig. 9). The maps are noisy because the Na X-ray count rates are low relative to other major elements, and only semi-quantitative because other compositional influences are not incorporated. However, if the uncertainty in the correlation between calculated pressure and measured Na content (Fig. 8) is considered acceptable, then the construction of pressure distribution maps is as plausible as mineral-liquid barometry applied to isolated spots. Moreover, the procedure is an improvement over a spot-only approach, because knowledge of the spatial distribution of compositional variation permits critical evaluation of its fidelity as a recorder of environmental conditions.

Inspection of the distributions of pressure values resulting from this procedure applied to two crystals (Fig. 9 insets) reveals important insights. Although the distributions overlap substantially, the spongy regions have modal pressure values that are consistently lower than those of the non-spongy regions (e.g., 400 vs. 630 MPa for Ka01-18, 530 vs. 650 MPa for Ka01-26, and 410 vs. 775 MPa for Ka02-04). This pattern is also consistent with the spatial distribution evident in the maps: spongy regions are more heterogeneous, but are distinctly different in hue from the smooth, non-spongy regions. The fact that the outermost rims represent substantively low pressures (consistently 0–200 MPa) than either of the two internal domains is consistent with the lower Na_2O observed in the spot analyses. However, the relationship between texture type (spongy vs. non-spongy) and pressure is not apparent from the spot analyses (Fig. 7), just as there is no apparent difference in the compositions of each texture type according to spot analysis-based element variation diagrams (Fig. 5).

Discussion

Evidently, the spatial information afforded by element mapping reveals correlations between texture and composition that are not detectable by analysis of what would

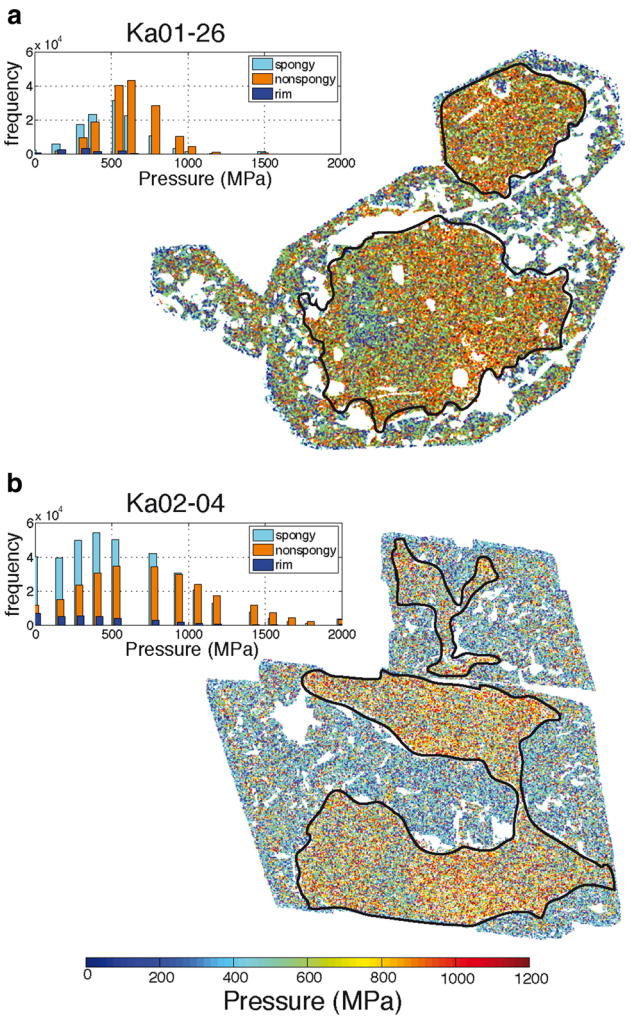

Fig. 9 Pressure maps generated from Na intensity maps for **a** Ka01-26 and **b** Ka02-04 utilizing correlation from Fig. 8. These images reveal subtle spatial correlation between texture type and calculated pressure not revealed by spot analyses. *Insets* are unnormalized frequency distributions of inferred pressures for spongy and non-spongy texture types and outermost rims

conventionally be considered a large number (≥30) of spots per crystal. We are now equipped to explore what additional insights regarding magmatic processes are suggested by the enhanced spatial context of compositional data and the derived thermobarometry results. Did the subtly lower-Na, lower-Al (Fig. 6) spongy portions of the Qkuls clinopyroxene crystals actually form at a lower pressure than the non-spongy portions? What is the significance of the spongy texture with respect to the thermodynamic stability of clinopyroxene? What, if any, barometric constraints may be plausibly imposed by the Qkuls samples, and do these constraints help resolve the depth debate that has been suggested by existing models of the postshield stage of Hawaiian volcanoes? We begin by considering the issue of the most likely scenarios of crystal growth conditions supported by the spatially contextualized compositional data, starting with the relevance of the Qkuls crystals in a larger context and whether the host lava accumulated clinopyroxene crystals prior to eruption.

Relevance of the crystals examined to Haleakala postshield magma

Whereas the Qkuls analyses come from 6 crystals collected from a single locality from within a single flow, the Chatterjee et al. (2005) data are collected from several dozen crystals in 11 flow units. In terms of the ranges in Mg, Na, Ti, Al, and Cr concentrations, intracrystal variation within the Qkuls samples is similar to the variation among all extant clinopyroxene analyses from Haleakala postshield lavas (Chen et al. 1990; Fodor et al. 1975). The Qkuls crystals appear to be typical in composition, and although crystal-by-crystal petrographic analysis is not available for these other postshield ankaramite lavas, we have no reason to suspect that Qkuls crystals are texturally unique either.

Cumulate ankaramite?

None of the analyzed clinopyroxene crystals are Mg-rich enough to be in Fe–Mg equilibrium with the Ka01 and Ka02 WR compositions; hence, the need to calculate points along the two L_{arrays} by mass balance. Subtraction of ~25 wt% crystals in the observed clinopyroxene: olivine ratio of 1.8:1 (Table 2) from the WR compositions is required to achieve Fe–Mg exchange equilibrium in the most Mg-rich clinopyroxene, and the least magnesian clinopyroxenes achieve Fe–Mg exchange equilibrium after subtraction of 45 wt% crystals (Table 5). Thus, we infer that the WR compositions represent magmas that accumulated at least 25 wt% and possibly 45 wt% mafic minerals. Considering the high crystallinities of Kolekole samples (Chatterjee et al. 2005), which, as scoriaceous pyroclasts, are incapable of post-eruption crystal accumulation (by flow segregation and/or crystal settling), it is likely that ankaramites at Haleakala ascend through the plumbing system having already accumulated crystals. It is therefore probable that most of the high crystallinities of our lava samples were established prior to magma ascent.

A large mass ratio of clinopyroxene to olivine, as observed in the ankaramite, may be considered supporting evidence for high pressure crystal fractionation because the clinopyroxene stability field increases relative to olivine as pressure increases between 1 atm and 700 MPa (Mahood and Baker 1986; Yoder and Tilley 1962). However, clinopyroxene saturation may actually follow olivine saturation in a liquid line of descent and still produce a clinopyroxenite if in situ crystallization locally accelerates liquid differentiation (Langmuir 1989). Successive horizons of

olivine-clinopyroxenite, wehrlite, and gabbros has been drilled in the layered series of Les Alizés volcano (Lerebour et al. 1989), and a similar layering has been inferred from gabbroic and ultramafic xenoliths at Mauna Kea (Fodor and Galar 1997). The presence of clinopyroxene: olivine in ~2:1 mass ratio in the ankaramite does not, by itself, constitute evidence for high magma crystallization pressure.

Thermobarometry: a critical evaluation

The combination of EPMA spot analyses and maps, along with mass balance constraints on putative liquid compositions and thermobarometric modeling, all point toward a wide range of compositions that suggest a range of pressures over which individual clinopyroxene crystals formed. Moreover, the calculated crystallization pressures obtained for spot analyses in Ka01-26 (Fig. 8; Table 5) are consistent with a relatively straightforward crystallization history: a high-Na clinopyroxene, non-spongy in texture, formed at high pressure (>700 MPa); it partially resorbed during exposure to disequilibrium conditions, possibly re-injection, and was transported to lower pressure (200–500 MPa) where an overgrowth of spongy-textured clinopyroxene mantled the resorbed core; finally, an outermost rim (~10 μm thick) crystallized at low pressure (0–60 MPa), possibly during eruption or emplacement of a lava flow. This interpretation pairs the assumptions underlying thermobarometry (chemical equilibrium) with logical geologic sequencing—that high-Na (high pressure) crystallization precedes low-Na (low pressure) crystallization. The spatial distribution of Na in crystal Ka01-26 conforms to this scenario because it contains a high-Na core, a moderate-Na mantle, and low-Na outermost rim, as ascertained by the Na element map (Fig. 9).

Applying the observed correlation between domain texture and composition (e.g., for Ka02-04 in Fig. 6 and for Ka01-26 and Ka01-18 in Fig. SM7), we evaluate whether this growth-ascent/dissolution-growth scenario is generally plausible for the Qkuls crystals. In fact, the vast majority of clinopyroxene crystals do not exhibit the same stratigraphy of non-spongy core/spongy mantle/outer rim as Ka01-26. For example, Ka01-30, Ka0-09, Ka01-18, Ka01-04, Ka02-13, and Ka02-04 have non-spongy regions with planar external facets in contact with matrix (Fig. 2). Thus, the patterns of high and low pressure are not consistent with simple core to rim development of individual crystals transiting the lithosphere from high to low pressure. Welsch et al. (2015) develop a case for growth at initially high undercooling as the cause of the spongy and non-spongy textural domains that characterize Qkuls clinopyroxene (Fig. 2a and SM1). They posit that growth sectors of the {hk0} family correspond to spongy domains within the crystal interiors,

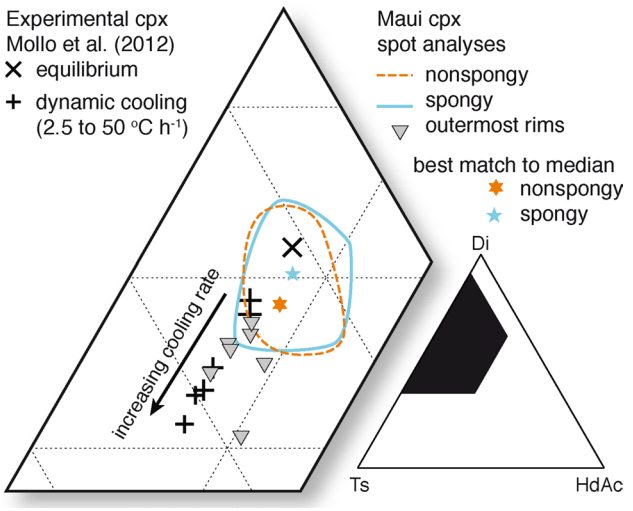

Fig. 10 Maui ankaramite clinopyroxene and crystals from dynamic cooling experiments (Mollo et al. 2013) in Di-Ts-HdAc ternary system. End members are defined as Di = 100-Ts-HdAc; Ts = ^{iv}Al; HdAc = Fe^{2+}+ Na, with components as determined using the method of Sturm (2002). In the experimental samples, Al in clinopyroxene increases as cooling rate increases from 2.5 to 50 °C, in the direction of the *arrow*

that the sectors under the *c*-axis intersecting {hk1} faces are non-spongy in texture, and that the variety of observed spatial distributions is consistent with sectioning effects. The elemental covariations exhibited by ankaramite clinopyroxene crystals (Fig. 5) are indeed consistent with a substitution reaction, $(Al + Ti)_{\{-111\}} = (Si + Mg)_{\{110\},\{100\},\{010\}}$, associated with sector zoning (Hollister and Gancarz 1971; Hollister and Hargraves 1970; Leung 1974; Strong 1969; Wass 1973), and indicative of growth at moderate to high undercooling (Kouchi et al. 1983). However, sector zoning as an explanation of spatial variation is not necessary to the main inference arising from this study, which is that the presence of compositional sub-domains within individual crystals jeopardizes the application of thermobarometry. The negative correlation between clinopyroxene Al_2O_3 content and computed pressure (typical for experimental systems; e.g., Fig. SM5d) is an additional indication that a magmatic process, not environmental condition, is responsible for the compositional variation.

We envision two possibilities: neither of the domain types is representative of chemical equilibrium between clinopyroxene and liquid, or one of the two domains is in equilibrium and the other is influenced by kinetic effects. To examine these possibilities, we consider the element partitioning shift observed in dynamic cooling experiments from 1250 to 1100 °C on a trachybasalt from Mt. Etna (SiO_2 = 49.71, Al_2O_3 = 15.34, FeO = 8.61, MgO = 7.04, CaO = 11.54, Na_2O = 3.84, K_2O = 1.40) of Mollo et al. (2013), which crystallizes clinopyroxene similar to those

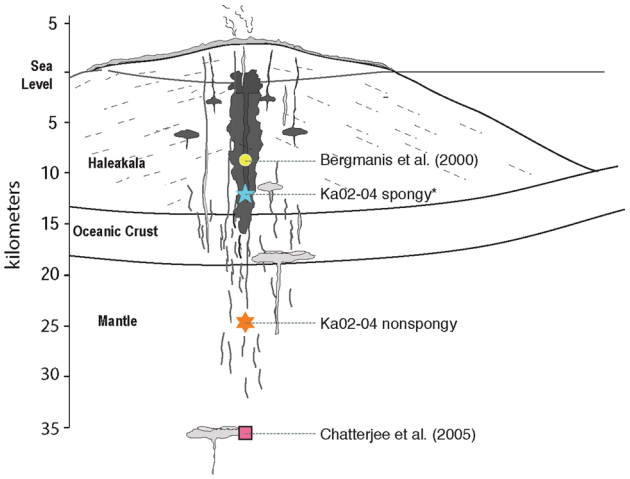

Fig. 11 Schematic illustration of the magma supply system operative during the volcano's shield stage (*dark gray*) and postshield stage (*light gray*), adopted from Moore (1987) and Wolfe et al. (1997), along with depth constraints from clinopyroxene thermobarometry (Chatterjee et al. 2005), liquid line of descent modeling (Bergmanis et al. 2000), and this study. *Stars* represent depths implied by median Na contents of the spongy and non-spongy subgrain domain types for crystal Ka02-04. The lower-pressure, crustal values are preferred for the reasons developed herein

in the Maui Qkuls samples. The clinopyroxene compositions produced at cooling rates from 2.5, 10, and 50 °C h^{-1} are projected into the Di-Hd-Ts ternary system (Huckenholz 1973), highlighting the major consequences of rapid crystal growth on crystal composition (Fig. 10). The Fe–Mg exchange coefficients of the Mollo et al. (2013) synthetic clinopyroxenes increase with increasing cooling rate, and thus FeO/MgO increases toward the Ts corner of the diagram (not shown). A positive correlation between cooling rate and nonstoichiometric components in clinopyroxene is also observed in the dynamic experiments performed at 500 MPa (Mollo et al. 2010). The clinopyroxene from Qkuls samples span an array that is coincident with the synthetic crystals formed at progressively rapid cooling, including FeO/MgO ratio that increases with Ts. In fact, the compositions of the outermost rims overlap with the fastest cooled synthetic crystals. Although the points representing spongy and non-spongy domains span indistinguishable clouds, our determination of the median compositions using element maps (Fig. 6 and SM4) permits selection of the two analyses most representative of each domain type; these are shown as stars. The median spongy composition is near the experimental composition representing equilibrium at 1150 °C, whereas the median non-spongy composition (slightly richer in Al_2O_3) is closer to the experimental crystals formed at a cooling rate of 2.5 °C h^{-1}. The comparison does not require that cooling rate in the Maui magma was similar to the laboratory values. The elemental variations occur due to rapid crystal growth, which does not require rapid cooling, (e.g., because of nucleation delay, thermal gradient, or crystal cycling; Faure et al. 2006; Welsch et al. 2013). However, it does suggest that if the composition of either domain represents chemical equilibrium with surrounding liquid, the conservative choice is probably the lower-Al_2O_3, lower-Na_2O analyses of the spongy domains, as suggested by Nimis and Ulmer (1998).

Given the uncertainties in liquid composition, sensitivity to thermobarometry model combinations, and manifest evidence for chemical disequilibrium associated with sector zoning in these crystals, our study reinforces the need to develop criteria for identifying and interpreting kinetic effects in the compositions of euhedral crystals. However, taking the values obtained as estimates, we contextualize them with other pressure/depth estimates for Haleakala postshield magmas in Fig. 11. Our application of clinopyroxene-liquid barometry indicates crystallization pressures of ~400 MPa for the spongy regions and 775 MPa for the non-spongy regions (for Ka02-04; Fig. 9), with the lower value being considered more plausible in view of arguments presented above. Taking 2400, 2800, 3000, and 3300 kg m^{-3} as the densities of the upper edifice, lower edifice, Cretaceous crust, and mantle, respectively, and Moho depth of 19 km below sea level at Haleakala (Moore 1987), these pressures correspond to depths of 12.6 and 24.6 km below the summit, respectively. Within barometric uncertainty, the more plausible of our Qkuls values is 4 km below the result of Bergmanis et al. (2000), which used thermodynamic modeling (Ghiorso and Sack 1995) to constrain the pressure of crystallization for a suite of whole-rock compositions. The less plausible of the Qkuls values is ~10 km shallower than the clinopyroxene-liquid thermobarometric result preferred by Chatterjee et al. (2005).

The preservation of delicate plagioclase laths protruding into some of the void spaces (Fig. 2d) suggests fluid saturation at the time of crystal growth and thus additional support for mid-edifice magma storage prior to eruption. Volatile saturation is far more likely at crustal pressures than mantle depths. Magma reservoir pressurization by exsolved volatiles may be essential for propelling crystal-rich mush to the surface, particularly in a summit eruption such as that which produced the Qkuls lava. An important role for volatiles is undeniable in the case of mildly explosive events such as that which produced the Kolekole cinder cone (Chatterjee et al. 2005). A final possibility is that the penetration of a volatile saturation front to the mushy margins of the magma reservoir, captured as true void space in growing clinopyroxene crystals, may coincide with attainment of reservoir overpressure that triggered magma ascent and eruption of the Qkuls lava.

Magma plumbing systems beneath postshield Hawaiian volcanoes

At Hawaiian volcanoes such as Mauna Kea, Hualalai, and Haleakala, ankaramites are typically erupted during a transition between the shield building stage, which is typified by the eruption of picritic and tholeiitic basalts, and the late postshield stage, dominated by differentiated alkalic lavas including hawaiites, mugearites and trachytes (Langenheim and Clague 1987; Wolfe et al. 1997). In the late part of shield magmatism, the immediate source of erupted material is inferred to be the same shallow, edifice-level reservoir recently occupied by tholeiitic magma. Erupted magma is relatively primitive and alkalic in character, owing to low extents of partial mantle melting. The composition of erupted magma in this period of declining magma throughput is increasingly alkalic, due to the relatively short time available for differentiation by crystal fractionation. As the volcano moves further from the hot spot, magma supply wanes and the shallow to mid-crustal reservoirs become thermally starved and eventually solidify. The feeding system deepens, extending to the base of the lithosphere or below. Eruption frequency declines, and the magmas that do erupt are highly differentiated and rich in volatiles. Differentiation and volatile enrichment presumably occurs because protracted residence in the plumbing system promotes crystal fractionation.

Several petrologic characteristics support this paradigm of postshield volcanism, including (a) a sharp temporal transition and substantial compositional gap between basaltic and differentiated (trachyte, mugearite) magmas (Frey et al. 1990; Macdonald and Katsura 1964; Naughton et al. 1980); (b) increasing dominance in the fractionating assemblage of clinopyroxene, a consequence of its increasing stability at high pressure relative to olivine (Mahood and Baker 1986; Yoder and Tilley 1962); (c) clinopyroxene-liquid thermobarometry having determined crystallization pressures up to 12 kbar (~40 km) for several postshield lavas (Putirka et al. 1996).

Our study shows, however, that thermobarometry yields ambiguous results when applied to spatially heterogeneous crystals such as those in Qkuls ankaramite. Assuming disequilibrium partitioning of pressure-sensitive species (Na and Al) into the $\{-111\}$ sectors, thermobarometry applied to the other sectors suggests that the interiors of the clinopyroxene crystals of Qkuls ankaramite crystallized in the lower crust. The chemical characteristics of Haleakala postshield magmas are influenced not only by the mantle source and melting conditions, but also by magma chamber processes occurring within the volcanic edifice. Our inference that postshield ankaramite is processed in the crust is corroborated by the presence of exclusively crustal xenoliths (and the absence of mantle xenoliths) in the postshield products of Hawaiian volcanoes (Clague and Sherrod 2014 and references therein).

Haleakala has sustained the longest postshield stage of any Hawaiian volcano (Sherrod et al. 2003), with a minimum duration of 930 ka (Chen et al. 1991; Sherrod et al. 2003), as compared with 70–250 ka for Mauna Kea (Macdonald and Powers 1968; Wolfe et al. 1997) and <133 ka for Hualalai (Moore and Clague 1992). Although magma supply declined through time at Haleakala, the outcrop-scale and crystal-scale petrologic data do not support disappearance of crustal magma reservoirs and transition to a sub-lithospheric source for postshield magmas at Haleakala. Our findings support a crustal, within-edifice origin for ankaramite lavas à la Bergmanis et al. (2000).

Conclusions

We posit that our very detailed investigation of several crystals is germane to Maui postshield ankaramites in general, and the factors controlling clinopyroxene composition may vary similarly from one Haleakala ankaramite to the next. Our application of clinopyroxene-liquid thermobarometric models yields ranges of crystallization temperature and pressure that are generally consistent with those of previous studies (Chatterjee et al. 2005), but conclude that combinations of thermometers and barometers yielding pressure values at the low end of the spectrum are most appropriate to the Haleakala ankaramite.

Mineral-liquid thermobarometry remains a valuable tool for evaluating intrinsic conditions of crystal-rich magmas. However, critically evaluating the applicability of such equilibrium-based models and reconciling different methods of determining crystallization pressure are essential if we are to interpret the volcanological significance of crystal-rich lavas such as ankaramites. We suggest that crystal-liquid thermobarometry applied to Haleakala clinopyroxene crystals yields anomalously high crystallization pressures (and temperatures), either because of sector zoning effects (Welsch et al. 2015), because rapid growth perturbs equilibrium partitioning of elements (Mollo et al. 2013), or both. Revised estimates of clinopyroxene crystallization pressure, in combination with evidence that the ankaramites are cumulates, suggest that the postshield stage of magmatic evolution at Haleakala has yet to deepen to sub-edifice levels, as has been posited on the basis of clinopyroxene-liquid thermobarometry and a similarity argument referencing Mauna Kea (Chatterjee et al. 2005; Wolfe et al. 1997). Rather, the textural evidence for an exsolved vapor phase and nearly identical compositional variations among crystals from diverse postshield magmas are consistent with magma differentiation by in situ crystallization (Langmuir 1989) within mid-crustal magma reservoirs.

Acknowledgments JoAnn Sinton is gratefully acknowledged for the loan of many loose crystals and for thin section preparation. Olivier Odon is also thanked for his help with the Haleakala DEM. The manuscript was improved with comments from reviewers Keith Putirka and Matteo Masotta. This work was supported by NSF EAR 12-20084 to JEH and is SOEST publication number 9529.

References

Baker DR, Eggler DH (1987) Compositions of anhydrous and hydrous melts coexisting with plagioclase, augite, and olivine or low-Ca pyroxene from 1 atm to 8 kbar: application to the Aleutian volcanic center of Atka. Am Mineral 72:12–28

Barsdell M (1988) Petrology and petrogenesis of clinopyroxene-rich tholeiitic lavas, Merelava Volcano, Vanuatu. J Petrol 29(5):927–964

Barsdell M, Berry RF (1990) Origin and evolution of primitive island arc ankaramites from Western Epi, Vanuatu. J Petrol 31(3):747–777

Bartels KS, Kinzler RJ, Grove TL (1991) High pressure phase relations of primitive high-alumina basalts from Medicine Lake volcano, northern California. Contrib Mineral Petrol 108(3):253–270. doi:10.1007/bf00285935

Beattie P (1993) Olivine-melt and orthopyroxene-melt equilibria. Contrib to Mineral Petrol 115:103–111. doi:10.1007/BF00712982

Bergmanis EC, Sinton JM, Trusdell FA (2000) Rejuvenated volcanism along the southwest rift zone, East Maui, Hawaii. Bull Volcanol 62(4–5):239–255. doi:10.1007/s004450000091

Chappell B (1992) Trace element analyses in rocks by X-ray spectrometry. Adv X-Ray Anal 34:263–276

Chatterjee N, Bhattacharji S, Fein C (2005) Depth of alkalic magma reservoirs below Kolekole cinder cone, Southwest rift zone, East Maui, Hawaii. J Volcanol Geotherm Res 145(1–2):1–22. doi:10.1016/j.jvolgeores.2005.01.001

Chen CY, Frey FA, Garcia MO (1990) Evolution of alkalic lavas at Haleakala Volcano, East Maui, Hawaii. Contrib Mineral Petrol 105(2):197–218. doi:10.1007/bf00678986

Chen CY, Frey FA, Garcia MO, Dalrymple GB, Hart SR (1991) The tholeiite to alkalic basalt transition at Haleakala Volcano, Maui, Hawaii. Contrib Mineral Petrol 106(2):183–200. doi:10.1007/bf00306433

Clague DA, Sherrod DR (2014) Growth and degradation of Hawaiian volcanoes. In: Poland MP, Takahashi TJ, Landowski CM (eds) Characteristics of Hawaiian volcanoes. US Geological Survey, Washington, DC, pp 97–146

Coombs DS, Wilkinson JFG (1969) Lineages and fractionation trends in undersaturated volcanic rocks from the East Otago volcanic province (New Zealand) and related rocks. J Petrol 10(3):440–501

Della-Pasqua FN, Varne R (1997) Primitive ankaramitic magmas in volcanic arcs; a melt-inclusion approach. Can Mineral 35(2):291–312

Eggins SM (1993) Origin and differentiation of picritic arc magmas, Ambae (Aoba) Vanuatu. Contrib Mineral Petrol 114(1):79–100. doi:10.1007/bf00307867

Faure F, Arndt N, Libourel G (2006) Formation of spinifex texture in komatiites: an experimental study. J Petrol 47(8):1591–1610

Fodor RV, Galar P (1997) A view into the subsurface of Mauna Kea volcano, Hawaii: crystallization processes interpreted through the petrology and petrography of gabbroic and ultramafic xenoliths. J Petrol 38(5):581–624

Fodor RV, Keil K, Bunch TE (1975) Contributions to the mineral chemistry of Hawaiian rocks. IV. Pyroxenes in rocks from Haleakala and West Maui volcanoes, Maui, Hawaii. Contrib Mineral Petrol 50(3):173–195. doi:10.1007/bf00371038

Frey FA, Wise WS, Garcia MO, West H, Kwon ST, Kennedy A (1990) Evolution of Mauna Kea Volcano, Hawaii: petrologic and geochemical constraints on postshield volcanism. J Geophys Res 95(B2):1271–1300. doi:10.1029/JB095iB02p01271

Genske FS, Turner SP, Beier C, Schaefer BF (2012) The petrology and geochemistry of lavas from the Western Azores Islands of Flores and Corvo. J Petrol 53(8):1673–1708

Georgiev S, Marchev P, Heinrich CA, Von Quadt A, Peytcheva I, Manetti P (2009) Origin of nepheline-normative high-K ankaramites and the evolution of Eastern Srednogorie arc in SE Europe. J Petrol 50(10):1899–1933

Ghiorso MS, Sack RO (1995) Chemical mass transfer in magmatic processes IV. A revised and internally consistent thermodynamic model for the interpolation and extrapolation of liquid-solid equilibria in magmatic systems at elevated temperatures and pressures. Contrib Mineral Petrol 119(2):197–212

Gunn BM, Coy-Yll R, Watkins ND, Abranson CE, Nougier J (1970) Geochemistry of an oceanite-ankaramite-basalt suite from East Island, Crozet Archipelago. Contrib Mineral Petrol 28(4):319–339. doi:10.1007/bf00388954

Helz RT (1987) Diverse olivine types in lava of the 1959 eruption of Kilauea volcano and their bearing on eruption dynamics. US Geol Surv Prof Pap 1350:691–722

Hollister LS, Gancarz AJ (1971) Compositional sector zoning in clinopyroxene from the Narce area, Italy. Am Mineral 56:950–979

Hollister LS, Hargraves RB (1970) Compositional zoning and its significance in pyroxenes from two coarse grained Apollo 11 samples. Proceedings of Apollo 11 Lunar Science conference, vol 1, pp 541–550

Huckenholz HG (1973) The origin of fassaitic augite in the alkali basalt suite of the Hocheifel area, Western Germany. Contrib Mineral Petrol 40(4):315–326. doi:10.1007/bf00371022

Kilinc A, Carmichael ISE, Rivers ML, Sack RO (1983) The ferric-ferrous ratio of natural silicate liquids equilibrated in air. Contrib Mineral Petrol 83(1–2):136–140. doi:10.1007/bf00373086

Kinzler RJ, Grove TL (1992) Primary magmas of mid-ocean ridge basalts 1. Experiments and methods. J Geophys Res 97(B5):2156–2202. doi:10.1029/91JB02840

Kohut EJ, Stern RJ, Kent AJR, Nielsen RL, Bloomer SH, Leybourne M (2006) Evidence for adiabatic decompression melting in the Southern Mariana Arc from high-Mg lavas and melt inclusions. Contrib Mineral Petrol 152(2):201–221. doi:10.1007/s00410-006-0102-7

Kornprobst J, Ohnenstetter D, Ohnenstetter M (1981) Na and Cr contents in clinopyroxenes from peridotites: a possible discriminant between "sub-continental" and "sub-oceanic" mantle. Earth Planet Sci Lett 53(2):241–254

Kouchi A, Sugawara Y, Kashima K, Sunagawa I (1983) Laboratory growth of sector zoned clinopyroxenes in the system CaMgSi2O6–CaTiAl2O6. Contrib Mineral Petrol 83(1):177–184

Lacroix A (1916) Sur quelques roches volcaniques mélanocrates des Possessions françaises de l'océan Indien et du Pacifique

Lacroix A (1923) Minéralogie de Madagascar. Challamel, Paris, p 49

Lanari P, Vidal O, De Andrade V, Dubacq B, Lewin E, Grosch EG, Schwartz S (2014) XMapTools: a MATLAB©-based program for electron microprobe X-ray image processing and geothermobarometry. Comput Geosci 62:227–240. doi:10.1016/j.cageo.2013.08.010

Lange RL, Carmichael ISE (1990) Thermodynamic properties of silicate liquids with emphasis on density, thermal expansion and compressibility. Rev Mineral Geochem 24(1):25–64

Langenheim VAM, Clague DA (1987) The Hawaiiian-Emperor volcanic chain. Part II. Stratigraphic framework of volcanic rocks

of the Hawaiian Islands. In: Decker RW, Wright TL, Stauffer PH (eds) Volcanism in Hawaii, US Geol. Surv. Prof. Pap. 1350, pp 55–84

Langmuir CH (1989) Geochemical consequences of in situ crystallization. Nature 340(6230):199–205

Lerebour P, Rançon JP, Auge T (1989) The Grand Brûlé exploration drilling: new data on the deep framework of the Piton de la Fournaise volcano. Part 2: secondary minerals. J Volcanol Geotherm Res 36(1–3):129–137

Leung IS (1974) Sector-zoned titanaugites: morphology, crystal chemistry, and growth. Am Mineral 59(1–2):127–138

Lindsley DH (1983) Pyroxene thermometry. Am Mineral 68:477–493

Macdonald GA (1978) Geologic map of the crater section of Haleakala National Park, Maui, Hawaii. In: US Department of Interior/US Geological Survey Miscellaneous Investigation Series, pp Map I-1088

Macdonald GA, Katsura T (1964) Chemical composition of Hawaiian lavas. J Petrol 5(1):82–133

Macdonald GA, Powers HA (1968) A further contribution to the petrology of Haleakala volcano, Hawaii. Geol Soc Am Bull 79(7):877–888

Macdonald GA, Abbot AT, Peterson FL (1983) Volcanoes in the sea. University of Hawaii Press, Honolulu

Mahood GA, Baker DR (1986) Experimental constraints on depths of fractionation of mildly alkalic basalts and associated felsic rocks: pantelleria, Strait of Sicily. Contrib Mineral Petrol 93(2):251–264. doi:10.1007/bf00371327

Marsh BD (1981) On the crystallinity, probability of occurrence, and rheology of lava and magma. Contrib Mineral Petrol 78(1):85–98

Mollo S, Del P, Ventura G et al (2010) Dependence of clinopyroxene composition on cooling rate in basaltic magmas: implications for thermobarometry. Lithos 118:302–312. doi:10.1016/j.lithos.2010.05.006

Mollo S, Blundy JD, Iezzi G, Scarlato P, Langone A (2013) The partitioning of trace elements between clinopyroxene and trachybasaltic melt during rapid cooling and crystal growth. Contrib Mineral Petrol 166(6):1633–1654. doi:10.1007/s00410-013-0946-6

Moore JG (1987) Subsidence of the Hawaiian Ridge. In: Volcanism in Hawaii, US Geol. Surv. Prof. Pap. 1350, pp 85–100

Moore JG, Ault WU (1965) Historic littoral cones in Hawaii. Pac Sci 19:3–11

Moore JG, Clague DA (1992) Volcano growth and evolution of the island of Hawaii. Geol Soc Am Bull 104(11):1471–1484

Morimoto N, Fabries J, Ferguson AK, Ginzburg IV, Ross M, Seifert FA, Zussman J, Aoki K, Gottardi G (1988) Nomenclature of pyroxenes. Mineral Mag 52:535–550

Naughton JJ, MacDonald GA, Greenberg VA (1980) Some additional potassium-argon ages of hawaiian rocks: the Maui volcanic complex of Molokai, Maui, Lanai and Kahoolawe. J Volcanol Geotherm Res 7(3–4):339–355. doi:10.1016/0377-0273(80)90037-2

Nimis P (1995) A clinopyroxene geobarometer for basaltic systems based on crystal-structure modeling. Contrib Mineral Petrol 121(2):115–125. doi:10.1007/s004100050093

Nimis P (1999) Clinopyroxene geobarometry of magmatic rocks. Part 2. Structural geobarometers for basic to acid, tholeiitic and mildly alkaline magmatic systems. Contrib Mineral Petrol 135(1):62–74

Nimis P, Taylor WR (2000) Single clinopyroxene thermobarometry for garnet peridotites. Part I. Calibration and testing of a Cr-in-Cpx barometer and an enstatite-in-Cpx thermometer. Contrib Mineral Petrol 139(5):541–554

Nimis P, Ulmer P (1998) Clinopyroxene geobarometry of magmatic rocks Part 1: an expanded structural geobarometer for anhydrous and hydrous, basic and ultrabasic systems. Contrib Mineral Petrol 133(1):122–135

Norrish K, Hutton JT (1969) An accurate X-ray spectrographic method for the analysis of a wide range of geological samples. Geochim Cosmochim Acta 33(4):431–453. doi:10.1016/0016-7037(69)90126-4

Ortiz Hernández LE (2000) An arc ankaramite occurrence in Central Mexico. Revista Mexicana de Ciencias Geológicas 17(1):34–44

Pietruszka AJ, Heaton DE, Marske JP, Garcia MO (2015) Two magma bodies beneath the summit of Kilauea Volcano unveiled by isotopically distinct melt deliveries from the mantle. Earth Planet Sci Lett 413:90–100. doi:10.1016/j.epsl.2014.12.040

Poland MP, Miklius A, Montgomery-Brown EK (2014) Magma supply, storage, and transport at shield-stage Hawaiian volcanoes. In: Poland MP, Takahashi TJ, Landowski CM (eds) Characteristics of Hawaiian volcanoes. US Geological Survey, Washington, D.C., pp 179–234

Putirka K (1999) Clinopyroxene + liquid equilibria to 100 kbar and 2450 K. Contrib Mineral Petrol 135(2):151–163

Putirka KD (2008) Thermometers and barometers for volcanic systems. Rev Mineral Geochem 69(1):61–120

Putirka K, Johnson M, Kinzler R, Longhi J, Walker D (1996) Thermobarometry of mafic igneous rocks based on clinopyroxene-liquid equilibria, 0–30 kbar. Contrib Mineral Petrol 123(1):92–108. doi:10.1007/s004100050145

Putirka KD, Mikaelian H, Ryerson F, Shaw H (2003) New clinopyroxene-liquid thermobarometers for mafic, evolved, and volatile-bearing lava compositions, with applications to lavas from Tibet and the Snake River Plain, Idaho. Am Mineral 88(10):1542–1554

Ryan MP (1987) Neutral buoyancy and the mechanical evolution of magmatic systems. In: Mysen BO (ed) Magmatic processes: Physicochemical principles; Special Publication No 1. The Geochemical Society, University Park, pp 259–287

Sherrod DR, Nishimitsu Y, Tagami T (2003) New K–Ar ages and the geologic evidence against rejuvenated-stage volcanism at Haleakala, East Maui, a postshield-stage volcano of the Hawaiian island chain. Geol Soc Am Bull 115(6):683–694

Sherrod DR, Hagstrum JT, McGeehin JP, Champion DE, Trusdell FA (2006) Distribution, 14C chronology, and paleomagnetism of latest Pleistocene and Holocene lava flows at Haleakalā volcano, Island of Maui, Hawai'i: a revision of lava flow hazard zones. J Geophys Res 111(B5):B05205. doi:10.1029/2005jb003876

Sherrod DR, Sinton JM, Watkins SE, Brunt KM (2007) Geologic map of the State of Hawai`i. In: US Geol Surv Open-File Report, http://pubs.usgs.gov/of/2007/1089/

Sinton JM (2005) Geologic mapping, volcanic stages and magmatic processes in Hawaiian volcanoes In: EOS (ed) Amer Geophys Union Trans. vol 86, pp V51A–1471

Sinton J, Grönvold K, Sæmundsson K (2005) Postglacial eruptive history of the Western Volcanic Zone, Iceland. Geochem Geophys Geosyst 6(12):Q12009. doi:10.1029/2005gc001021

Stearns HT, Macdonald GA (1942) Geology and ground-water resources of the island of Maui, Hawaii. Hawaii Div Hydrography Bull: 7344

Strong DF (1969) Formation of the hour-glass structure in augite. Mineral Mag 37(288):472–479

Sturm R (2002) PX-NOM—an interactive spreadsheet program for the computation of pyroxene analyses derived from the electron microprobe. Comput Geosci 28(4):473–483. doi:10.1016/S0098-3004(01)00083-8

Tilling RI, Kauahikaua J, Brantley SR, Neal C (2014) The Hawaiian volcano observatory—a natural laboratory for studying basaltic volcanism. In: Poland MPTTJ, Landowski CM (eds) Characteristics of Hawaiian Volcanoes. US Geological Survey, Washington, D.C., pp 2–64

Wass SY (1973) The origin and petrogenetic significance of hour-glass zoning in titaniferous clinopyroxenes. Mineral Mag 39(302):133–144. doi:10.1180/minmag.1973.039.302.01

Welsch B, Faure F, Famin V, Baronnet A, Bachèlery P (2013) Dendritic crystallization: a single process for all the textures of olivine in basalts? J Petrol 54(3):539–574

Wolfe EW, Wise WS, Dalrymple GB (1997) The geology and petrology of Mauna Kea Volcano, Hawaii; a study of postshield volcanism. US Geol Surv Prof Pap 1557

Welsch B, Hammer JE, Baronnet A, Jacob S, Hellebrand E, Sinton J (2015) Clinopyroxene in postshield Haleakala ankaramite. 2. Texture, compositional zoning and supersaturation in the magma. Contrib Mineral Petrol. doi:10.1007/s00410-015-1213-9

Yoder HS, Tilley CE (1962) Origin of basalt magmas: an experimental study of natural and synthetic rock systems. J Petrol 3(3):342–532